Stochastic Dynamics of Lagrangian Pore-Scale Velocities in Three-Dimensional Porous Media

Alexandre Puyguiraud, Philippe Gouze, Marco Dentz

Stochastic Dynamics of Lagrangian Pore-Scale Velocities in Three-Dimensional Porous Media

Alexandre Puyguiraud[1,2], Philippe Gouze[2], and Marco Dentz[1]

[1]Spanish National Research Council (IDAEA-CSIC), Groundwater Hydrology Group (GHS), Barcelona, Spain, [2]Géosciences Montpellier, CNRS-Université de Montpellier, Montpellier, France

Abstract Upscaling dispersion, mixing, and reaction processes from the pore to the Darcy scale is directly related to the understanding of the dynamics of pore-scale particle velocities, which are at the origin of hydrodynamic dispersion and non-Fickian transport behaviors. With the aim of deriving a framework for the systematic upscaling of these processes from the pore to the Darcy scale, we present a detailed analysis of the evolution of Lagrangian and Eulerian statistics and their dependence on the injection condition. The study is based on velocity data obtained from computational fluid dynamics simulations of Stokes flow and advective particle tracking in the three-dimensional pore structure obtained from high-resolution X-ray microtomography of a Berea sandstone sample. While isochronously sampled velocity series show intermittent behavior, equidistant series vary in a regular random pattern. Both statistics evolve toward stationary states, which are related to the Eulerian velocity statistics. The equidistantly sampled Lagrangian velocity distribution converges on only a few pore lengths. These findings indicate that the equidistant velocity series can be represented by an ergodic Markov process. A stochastic Markov model for the equidistant velocity magnitude captures the evolution of the Lagrangian velocity statistics. The model is parameterized by the Eulerian velocity distribution and a relaxation length scale, which can be related to hydraulic properties and the medium geometry. These findings lay the basis for a predictive stochastic approach to upscale solute dispersion in complex porous media from the pore to the Darcy scale.

1. Introduction

Understanding the dynamics of pore-scale flow and transport is a central issue for the modeling and upscaling of porous media phenomena and processes from the pore to the Darcy scale such as hydrodynamic dispersion, the filtration of bacteria and colloids, and the mixing of dissolved chemicals and reactions between them. The sound upscaling of these processes and their modeling on the Darcy scale contribute to the understanding of the hydrodynamics of porous media and play an important role in environmental and industrial applications such as groundwater and soil remediation, the assessment of geological gas and waste storage, geothermal energy, and petroleum production.

Pore-scale flow heterogeneity is the cause of hydrodynamic dispersion but also of preasymptotic non-Fickian transport. These phenomena are directly linked to Lagrangian velocity statistics. In fact, dispersion in heterogeneous flows such as turbulent flow and flow through heterogeneous porous media is quantified in terms of the covariance of Lagrangian velocities (Dagan, 1987; Taylor, 1921). Preasymptotic behaviors such as early and late solute arrivals compared to Fickian predictions and nonlinear scaling of solute dispersion (Berkowitz & Scher, 2001; Becker & Shapiro, 2003; De Anna et al., 2013; Gouze et al., 2008; Kang et al., 2014; Levy & Berkowitz, 2003; Scher et al., 2002) can be traced back to particle retention in low-velocity zones and fast transport in regions of high velocities, which give rise to broad distributions of solute residence times. The Fickian limit may be approached only at time values that are much larger than the largest residence times (Dentz et al., 2004; Bijeljic & Blunt, 2006). The concept of residence or transition times in the modeling of pore-scale particle motion was employed in the pioneering studies of de Josselin de Jong (1958) and Saffman (1959). The models proposed by these authors are similar to time-domain and continuous time random walk approaches (Delay et al., 2005; Berkowitz et al., 2006; Noetinger et al., 2016; Painter & Cvetkovic, 2005) in that they consider particle motion through transitions over the characteristic pore lengths characterized by random time increments that depend on the distribution of pore-scale velocities. Recent experimental and numerical studies have shown that the occurrence of non-Fickian particle disper-
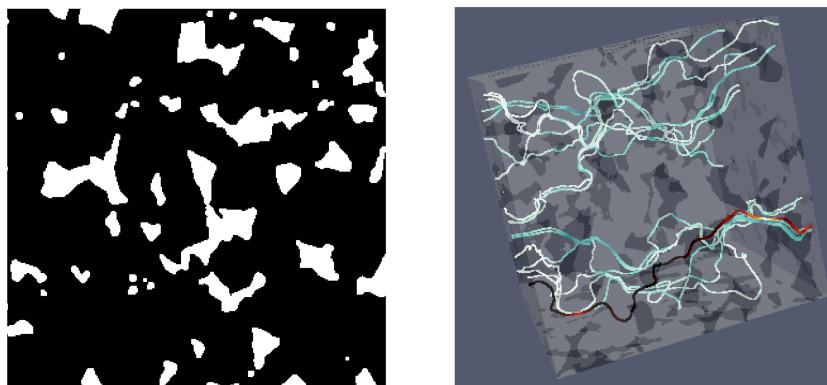
Figure 1. (left panel) Numerical cross section cropped in the Berea sandstone sample used for the flow simulations. White and black colors denote the pore space and the solid phase, respectively. (right panel) 3-D sample volume with 20 particle streamlines. Dark gray and light gray colors denote the pore space and the solid phase, respectively. The color scale of the streamlines denotes the velocity magnitude; from white for low-velocity values to blue for high-velocity values. The streamline colored from black to red is the one for which the space and time velocity series is reported in Figure 2.

sion due to long advective residence times is directly linked to intermittency in the Lagrangian velocity time series (Carrel et al., 2018; De Anna et al., 2013; Holzner et al., 2015; Kang et al., 2014; Morales et al., 2017). Thus, the understanding of these phenomena requires a sound characterization and understanding of the dynamics of Lagrangian and Eulerian pore-scale velocities, which have been the subject of a series of recent studies (De Anna et al., 2013; Gjetvaj et al., 2015; Holzner et al., 2015; Jin et al., 2016; Meyer & Bijeljic, 2016; Morales et al., 2017; Matyka et al., 2016; Siena et al., 2014).

It is frequently assumed that the velocity statistics obtained in experiments and numerical simulations are stationary, implying that they do not evolve in time. The experimental particle tracking velocimetry data of Morales et al. (2017) have shown that the distribution of initial particle velocities can in fact differ from the stationary velocity distribution depending on the injection volume and injection mode. This means that the velocity distribution evolves in time, depending on the initial particle placement within the sample. The dependence of the Lagrangian velocity statistics on the initial particle velocity distribution was studied by Le Borgne et al. (2007) for Darcy-scale flow and by Dentz et al. (2016) in a theoretical work and analyzed by Hyman et al. (2015) and Kang et al. (2017) for particle motion in random fracture networks. Based on experimental particle tracking velocimetry data from three-dimensional bead packs, Morales et al. (2017) analyzed particle velocities sampled equidistantly along particle trajectories, which removes the intermittency observed for isochronous velocity series. These authors model the mean and displacement variance as well as the velocity increment statistics based on a Markov model for equidistant velocities. The evolution of equidistant velocity series reflects the spatial organization of a steady flow field in that they vary on the characteristic heterogeneity length scales. Shapiro and Cvetkovic (1988) and Cvetkovic et al. (1991) proposed to analyze equidistant velocities as a basis to systematically quantify flow and travel time statistics in heterogeneous media (see, also, Gotovac et al., 2009; Le Borgne et al., 2007).

The presented study is based on pore-scale velocity data obtained for flow in a three-dimensional Berea sandstone sample, whose structure has been imaged by high-resolution X-ray microtomography (Figure 1). We systematically quantify the evolution of particles moving along streamlines both in time (isochronous sampling) and distance (equidistant sampling) and study the effect of the injection conditions. We provide explicit relations between the different statistics and discuss the issues of ergodicity and stationarity of the measured velocity series in time and distance, and the impact of the finiteness of the rock sample under consideration. The insights gained from this analysis lay the basis for the stochastic description of the equidistantly sampled velocity series in terms of an ergodic Markov chain. We consider three different stochastic models and study their capability of predicting the evolution of the Lagrangian velocity statistics. The impact of diffusion on pore-scale particle motion is discussed in section 5 (see, also, Bijeljic & Blunt, 2006; Dentz et al., 2018; Most et al., 2016).

The paper is organized as follows. Section 2 presents the methodology underlying this study. It details the flow and particle transport equations, summarizes briefly the acquisition and segmentation of the rock

sample, and explains the numerical solution method for the flow and particle tracking problems. Section 3 provides a comprehensive analysis of the statistics of the Lagrangian velocity magnitude both in time and distance. Then, we discuss the relations among them as well as their evolution toward stationarity. Section 4 investigates the capability of Markov models for predicting the stochastic dynamics of Lagrangian velocities. The conclusions on the stochastic description of the spatially sampled Lagrangian velocity dynamics as an ergodic Markov chain and the implications on the upscaling of preasymptotic hydrodynamic transport are given in section 5.

2. Methodology

In this paper, we analyze the statistical properties of Lagrangian velocities for purely advective transport in pore-scale flows. Pore-scale flow in general is governed by the Navier-Stokes equation. For the pore-scale flow scenarios under consideration here, the Reynolds number $Re = v_c \ell_p / \nu$, with a characteristic pore velocity v_c, a characteristic pore length ℓ_p, and the kinematic viscosity ν, is smaller than 1. Thus, the pore-scale flow velocity or Eulerian velocity $\mathbf{v}(\mathbf{x})$ can be obtained by solving the Stokes equation

$$\nabla^2 \mathbf{v}(\mathbf{x}) = \frac{1}{\nu} \nabla p(\mathbf{x}),$$ (1)

where $p(\mathbf{x})$ is the fluid pressure. Conservation of volume is expressed by $\nabla \cdot \mathbf{v}(\mathbf{x}) = 0$. We specify constant pressure at the inlet and outlet boundaries and no slip at the void-solid boundaries and the remaining domain boundaries. The porous rock sample and numerical solution of the pore-scale flow problem are described in sections 2.1 and 2.2.1 below.

The trajectory $\mathbf{x}(t, \mathbf{a})$ of a particle that is initially located at $\mathbf{x}(t = 0, \mathbf{a}) = \mathbf{a}$ is given by the advection equation

$$\frac{d\mathbf{x}(t, \mathbf{a})}{dt} = \mathbf{v}[\mathbf{x}(t, \mathbf{a})].$$ (2)

The Lagrangian velocity in the following is denoted by $\mathbf{v}(t, \mathbf{a}) = \mathbf{v}[\mathbf{x}(t, \mathbf{a})]$ and its magnitude by $v_t(t, \mathbf{a}) = \|\mathbf{v}[\mathbf{x}(t, \mathbf{a})]\|$. The initial velocity magnitude is denoted by $v(t = 0, \mathbf{a}) = v_0(\mathbf{a})$. The Eulerian velocity magnitude is denoted by $v_e(\mathbf{x}) = \|\mathbf{v}[\mathbf{x}]\|$. The distribution of initial particle positions is denoted by $\rho(\mathbf{a})$. We consider here two different initial distributions at the inlet plane at $x_1 = 0$. The uniform distribution spreads particles uniformly in the pore space; this means

$$\rho(\mathbf{a}) = \frac{\mathbb{I}_{\Omega_0}(\mathbf{a})}{V_0},$$ (3)

where Ω_0 denotes the domain in which particles are injected and V_0 its volume. The indicator function $\mathbb{I}_{\Omega_0}(\mathbf{a})$ is equal to 1 if $\mathbf{a} \in \Omega_0$ and 0 otherwise. This injection condition represents the initial condition of a spatially uniform concentration distribution. The flux-weighted initial distribution distributes particles weighted by their initial velocity as

$$\rho(\mathbf{a}) = \frac{v_0(\mathbf{a}) \mathbb{I}_{\Omega_0}(\mathbf{a})}{\int_{\Omega_0} v_0(\mathbf{a}) d\mathbf{a}}.$$ (4)

This injection condition represents a constant finite concentration pulse in the injection plane, such that the number of injected particles is proportional to the local flow velocity. The numerical particle tracking method is described in section 2.2.2. Before, however, we discuss the methodology of streamwise velocity sampling for the statistical analysis of Lagrangian velocity magnitudes.

2.1. Rock Sample

The analysis of the velocity field was performed using a volume of 0.95 mm^3 cropped into a digital representation of a Berea sandstone (Upper Berea Sandstone unit, Ohio, USA) core sample of length 10 mm and diameter 6 mm. The Berea sandstone is a (quarried) sedimentary rock composed of well-sorted quartz grains held together by silica-rich cement displaying intermediate porosity and permeability values as well as intermediate pore-scale structural heterogeneity (tortuosity, pore size distribution, etc.) of the pore network compared to standard reservoir rocks, while showing remarkable macroscopic homogeneity. Because of this, it is a "rock standard" which is widely used as a proxy of mildly heterogeneous rock for experimental works by academic and petroleum industry, and thus, results can be easily compared (e.g., Bijeljic et al.,

2004, 2011; Gjetvaj et al., 2015). Furthermore, the characteristics of the pore size distribution compared to both the imagery technique resolution and the image size limitation for Navier-Stokes simulations make this material ideal for investigating a mildly heterogeneous natural material. The image was acquired at the BM5 beamline at the European Synchrotron Radiation Facility (Grenoble, France) using X-ray microtomography. The 3-D volume was reconstructed from 3,495 X-ray projections using the single distance phase retrieval algorithm (Paganin et al., 2002; Sanchez et al., 2012). Since the Berea sandstone is a monocrystalline rock, we were able to relate the gray scale X-ray absorption directly to the porosity and transform the images into binary images (void and solid) using segmentation processes (Smal et al., 2018). The details of the data processing can be found in Gjetvaj et al. (2015). The cubic subset of 300^3 voxels was fine-grained (each voxel was divided by 3 in each direction) giving 900^3 voxels of volume 1.05 μm^3. The characteristic pore length is $\ell_p = 1.5 \cdot 10^{-4}$ m.

2.2. Numerical Simulations
2.2.1. Flow
Details of the flow simulation can be found in Gjetvaj et al. (2015). For completeness, we summarize them in this section. Generating the computational mesh that discretizes the geometry usually encounters two main problems. The first one is to create a mesh that is equivalent to the real digitized images, while the second is to make it fine enough to get a high resolution of the flow field. In order to avoid the smoothing and averaging procedure that often takes place in the OpenFOAM mesh creation, we use an algorithm that generates a mesh composed of cubes that fit exactly the voxels of the digitized sample. To obtain a fine resolution, we divide every 3-D cell of the mesh in 27 cubes resulting in a size of 1.05 μm^3 for each cell.

Then we compute the single-phase pore-scale flow by solving the Stokes and continuity equations for constant viscosity and density. The equations are solved via a finite volume scheme using the SIMPLE algorithm of OpenFOAM. This algorithm, based on a pressure-velocity coupling, solves the Stokes equation iteratively and allows us to obtain steady state pressure and velocity fields. Convergence is reached when the difference between the current and the previous step is smaller than a criterion.

Flow is solved by imposing pressure boundary conditions at the inlet and at the outlet. No-slip conditions are implemented at the interfaces of the solid phase and at the boundaries of the domain. We also add 20 layers at the inlet and at the outlet of the domain to minimize boundary effects. Once convergence is reached, we extract the velocity field. The velocity values are obtained at each interface of the voxelized mesh, in the normal direction. The computed Eulerian mean velocity is $\langle v_e \rangle = 8.05 \cdot 10^{-4}$ m/s. The characteristic pore length and the Eulerian mean velocity define the characteristic time scale $\tau_c = \ell_p / \langle v_e \rangle$.

2.2.2. Particle Tracking
The numerical solution of equation (2) for the particle trajectories, or, equivalently, streamlines of the pore-scale flow field, requires the interpolation of the flow velocities, which are defined at the faces of the finite volume voxels. Linear interpolation of each velocity component between opposing faces is volume preserving; this means $\nabla \cdot \mathbf{u}(\mathbf{x})$ inside each voxel. Linear interpolation has been used for particle tracking in Darcy-scale heterogeneous flow fields on a routine basis (Pollock, 1988). However, Mostaghimi et al. (2012) found that the linear interpolation does not respect the no-slip boundary condition at the void-solid interface. Thus, in the void voxels in contact with the solid voxels these authors replaced the linear by a quadratic velocity interpolation, which is the implementation employed here to interpolate velocity values in the void voxels. Particle trajectories are simulated until exiting the physical domain or reaching a given distance or a given elapsed time (Figure 1). The particle tracking solver probes the velocity statistics using regular sampling in space or time along the streamline as described in section 3.1.

In order to study particle displacements larger than the longitudinal sample size, particles are reinjected at the inlet boundary when they leave the flow domain at the outlet. The reinjection is processed as follows. When a given particle reaches the end of the domain at $x_1 = L$, its velocity magnitude $v_L(\mathbf{a}) = v_t(t, \mathbf{a})|_{x_1(t, \mathbf{a}) = L}$ is computed. Then, the pore space Ω_{v_0} at the inlet plane where the flow velocity magnitude values are $v_0 = \|\mathbf{u}(\mathbf{x})|_{x_1 = 0}\| \in [v_L(\mathbf{a}) - \Delta v, v_L(\mathbf{a}) + \Delta v]$ is identified and the particle is reinjected randomly in Ω_{v_0}, $\Delta v \approx \frac{v_L(\mathbf{a})}{200}$. This procedure guarantees continuity of velocity and velocity statistics at reinjection and makes sure that particle velocities do not decorrelate artificially. As reported in the following the evolution of Lagrangian
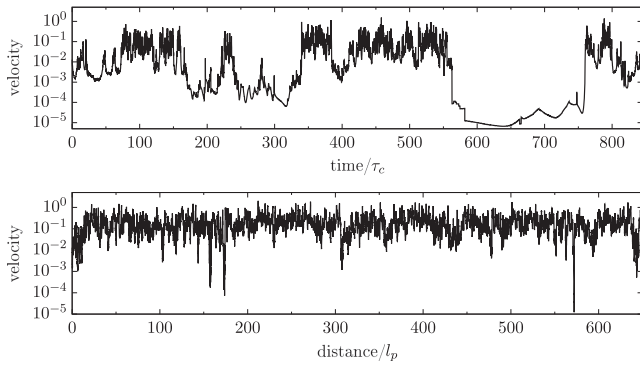
Figure 2. Time and space velocity magnitude series of a particle traveling through the sample. The series are computed following the streamline sampled either in time or in space. Velocity values sampled at constant time step display intermittency, whereas low- and high-velocity values last for comparable values of distance corresponding to about one pore length ℓ_p. The characteristic time is $\tau_c = \ell_p/\langle v_e \rangle$.

velocity statistics toward their respective steady state is not affected by reinjection in the sense that there is no noticeable acceleration due to a potential artificial decorrelation.

3. Lagrangian and Eulerian Velocity Statistics

In this section we introduce and discuss the Eulerian and Lagrangian velocity statistics used to analyze and understand pore-scale particle motion. We define velocity statistics sampled isochronously and equidistantly along streamlines and the relations between them. We first give a brief account of the literature on Lagrangian velocities and their use. The concept of isochronously sampled particle velocities was used by Taylor (1921) to quantify diffusion by continuous movements, more specifically by turbulent motion. A detailed statistical characterization of isochronous Lagrangian and Eulerian velocities was introduced by Lumley (1962). Shapiro and Cvetkovic (1988) proposed and analyzed the statistics of Lagrangian velocities sampled equidistantly along the mean flow direction. Le Borgne et al. (2007) considered the evolution of the probability density function (PDF) of such Lagrangian velocities, and Gotovac et al. (2009) used them as the basis to analyze flow and travel time statistics in heterogeneous porous media. Cvetkovic et al. (1991) compared isochronously and equidistantly sampled Lagrangian velocities for one-dimensional steady flow, Cvetkovic et al. (2012) for spatiotemporally varying flow. Recently, the statistics of isochronously sampled Lagrangian velocity were analyzed for pore-scale particle motion (De Anna et al., 2013; Kang et al., 2014; Meyer & Bijeljic, 2016; Siena et al., 2014), which are directly related to the particle dispersion (Kubo et al., 1991; Taylor, 1921). Dentz et al. (2016) and Morales et al. (2017) considered particle velocities sampled equidistantly along trajectories, which reflects the spatial organization of pore-scale flow. In the following we detail different methods to sample velocity statistics and their properties.

3.1. Streamwise Velocity Sampling

We consider two sampling methods to characterize particle velocities along the streamlines: isochronous and equidistant. First, the t(ime)-Lagrangian velocity magnitude or speed is defined as $v_t(t, \mathbf{a}) \equiv \|\mathbf{v}[\mathbf{x}(t, \mathbf{a})]\|$. The velocity time series $\{v_t(i\Delta t, \mathbf{a})\}_{i=0}^{\infty}$, with Δt being a constant time increment, is obtained by isochronous sampling along a particle trajectory. Meyer and Bijeljic (2016) modeled the Lagrangian velocity time series as Markov processes in order to quantify particle motion in heterogeneous velocity fields. Yet, isochronous velocity series in steady heterogeneous flow fields have been shown to display intermittency (De Anna et al., 2013; Kang et al., 2014). Figure 2 shows an isochronously sampled velocity series. It is characterized by long periods of low-velocity values and short peaks of high-velocity values. The origin of this intermittent behavior lies in the spatial organization of the flow.

The steady Eulerian velocity field varies on a length scale of the order of the average pore length ℓ_p. Thus, significant changes of the flow velocity along a trajectory occur at times ℓ_p/v. This explains the temporal persistence of low-velocity magnitudes and high frequency of change of high flow velocities. In order to account for the spatial organization of the velocity field, we consider particle velocities sampled equidistantly along trajectories (Dentz et al., 2016; Morales et al., 2017). The travel distance $s(t)$ along a particle trajectory is given by

$$\frac{\mathrm{d}s(t, \mathbf{a})}{\mathrm{d}t} = v_t(t, \mathbf{a}). \tag{5}$$

Performing the variable transform $t \to s$ in (2) gives the following set of equations describing the particle trajectory:

$$\frac{\mathrm{d}\mathbf{x}(s, \mathbf{a})}{\mathrm{d}s} = \frac{\mathbf{v}[\mathbf{x}(s, \mathbf{a})]}{\|\mathbf{v}[\mathbf{x}(s, \mathbf{a})]\|}, \quad \frac{\mathrm{d}t(s, \mathbf{a})}{\mathrm{d}s} = \frac{1}{v_s(s, \mathbf{a})}. \tag{6}$$
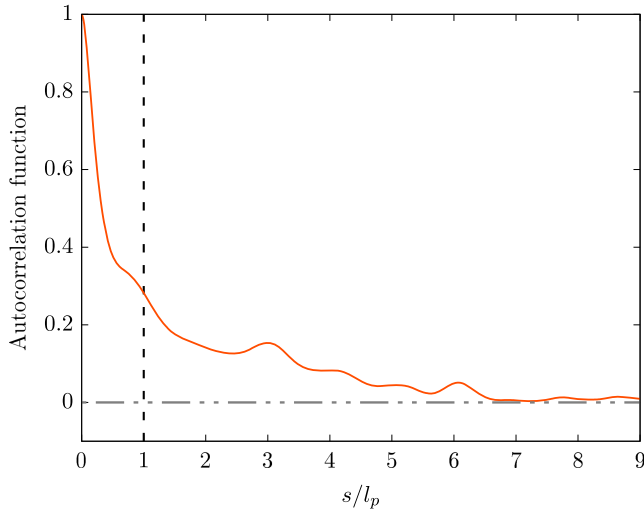
Figure 3. Autocorrelation function of the s-Lagrangian velocity $v_s(s)$.

The s-Lagrangian velocity magnitude is defined by $v_s(s) \equiv \|\mathbf{v}[\mathbf{x}(s, \mathbf{a})]\|$. The initial speed is denoted by $v_s(s = 0, \mathbf{a}) = v_0(\mathbf{a})$. The velocity series $\{v_s(i\Delta s, \mathbf{a})\}$, with Δs being a constant space increment, is obtained by equidistant sampling along particle trajectories. Unlike for isochronous sampling, here velocities are sampled independently of their magnitude since this velocity value does not impact the sampling distance. Note that the system of equations (6) describes particle motion as a process in which the particle position is incremented by a constant value and the particle time by a variable transition time. In this sense it describes a time-domain random walk (Noetinger et al., 2016).

The s-Lagrangian velocity series shown in Figure 2 does not display intermittent patterns. The signal seems stationary and is characterized by a characteristic correlation scale ℓ_v. To determine this correlation distance, we consider the velocity covariance function for an injection into the flux, which is defined as

$$C_v(s) = \frac{1}{L} \int \int_0^L \rho(\mathbf{a}) \left[v_s(s' + s, \mathbf{a}) - \mu\right] \left[v_s(s', \mathbf{a}) - \mu\right] ds' d\mathbf{a}, \quad (7)$$

where $\rho(\mathbf{a})$ is given by (4) and μ is the mean velocity

$$\mu = \frac{1}{L} \int \int_0^L \rho(\mathbf{a}) v_s(s', \mathbf{a}) ds' d\mathbf{a}. \quad (8)$$

The velocity autocorrelation function $\mathcal{A}_v(s) = C_v(s)/C_v(0)$ is shown in Figure 3. The correlation length is defined as

$$\ell_v = \int_0^\infty \mathcal{A}_v(s) ds. \quad (9)$$

We find that the velocity correlation length ℓ_v equals the average pore length, $\ell_p = 1.5 \cdot 10^{-4}$m. Note that the sample size is about $(6\ell_p)^3$ and that the average streamline length is around $10.5\ell_p$ which corresponds to an average tortuosity of 1.75.

The first series of Figure 2 illustrates the traditional temporal velocity sampling used for the computation of the velocity PDF. The statistics of the velocity magnitude $v_t(t, \mathbf{a})$ can be characterized by isochronous sampling along a single streamline labeled by $\mathbf{a}$. This sampling mode defines the streamwise t-Lagrangian velocity PDF $\hat{\mathcal{P}}(v, T, \mathbf{a})$

$$\hat{\mathcal{P}}(v, T, \mathbf{a}) = \frac{1}{T} \int_0^T \delta[v - v_t(t, \mathbf{a})] dt, \quad (10)$$

which in general depends on the sampling time T. In the following, the statistics obtained by isochronous sampling are marked by a hat. The statistics of the velocity series $v_s(s, \mathbf{a})$ illustrated in the bottom panel of Figure 2 is characterized by equidistant sampling,

$$\mathcal{P}(v, L, \mathbf{a}) = \frac{1}{L} \int_0^L \delta[v - v_s(s, \mathbf{a})] ds, \quad (11)$$

where L is the sampling length. The PDF $\mathcal{P}(v, L, \mathbf{a})$ is referred to in the following as streamwise s-Lagrangian velocity PDF. The relation between the streamwise s- and t-Lagrangian velocity PDFs defined in (11) and (10) is obtained by the variable change $s \to t$ according to the map (5), which gives

$$\mathcal{P}(v, L, \mathbf{a}) = \frac{vT(L)}{L} \hat{\mathcal{P}}[v, T(L), \mathbf{a}], \quad (12)$$
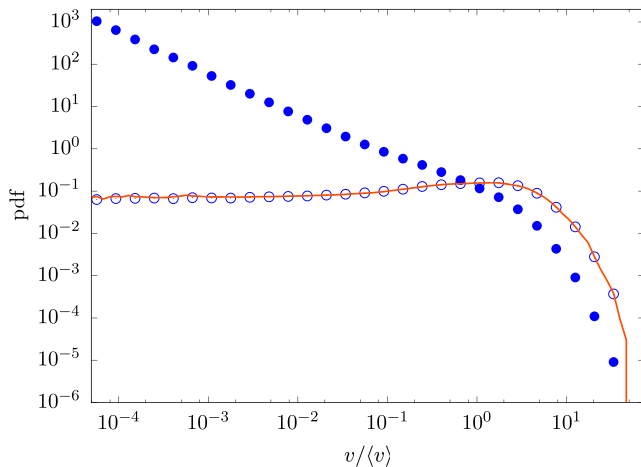

Figure 4. Streamwise t-Lagrangian PDF $\hat{\mathcal{P}}(v)$ (full circles), s-Lagrangian PDF $\mathcal{P}(v)$ (open circles), and the flux-weighting relation (17) (solid line). PDF = probability density function.
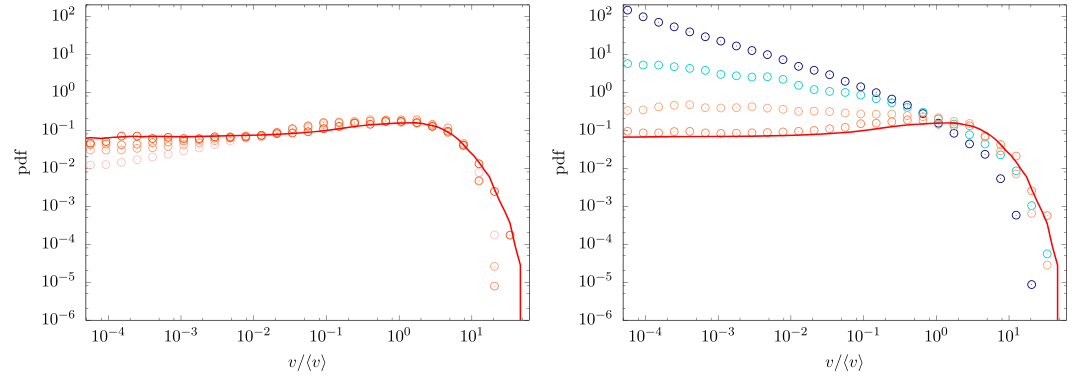
Figure 5. (left panel) Spatial evolution of the ensemble s-Lagrangian PDF $P(v, s)$ from the flux-weighted initial particle distribution $p_0(v)$ (pink open circles) to the steady s-Lagrangian PDF $P(v)$ (red solid line) at distances $s = 0, 1/5, 2/5, 5 \ell_p$. (right panel) Spatial evolution of the ensemble s-Lagrangian PDF $P(v, s)$ from the uniform initial particle distribution $p_0(v)$ (navy blue open circles) to the steady s-Lagrangian PDF $P(v)$ (red solid line) at distances $s = 0, 4/3, 4, 8 \ell_p$. The results were computed using 10^7 particles. PDF = probability density function.

where $T(L)$ is the time that the particle needs to travel the distance L along the streamline and

$$T(L) = \int_0^L \frac{\mathrm{d}s}{v_s(s)}. \tag{13}$$

Thus, the streamwise s- and t-Lagrangian PDFs are linked through flux weighting. This relation is purely kinematic and holds always. Figure 4 illustrates the streamwise s- and t-Lagrangian statistics as well as the flux-weighting relation for the rock sample under consideration. The velocity statistics along a single streamline are computed for a distance of $L \approx 10^8 \ell_p$ and corresponding duration of $T(L) \approx 9 \cdot 10^7 \tau_c$, where τ_c is the time for a particle to travel the distance ℓ_p by the average Eulerian velocity $\langle v_e \rangle$.

Therefore, under ergodic conditions, the velocity statistics sampled between an ensemble of particles and along a single streamline are equivalent. Ergodicity can only be achieved if first, the sampling distance or sampling time along a streamline is large enough for the particle to experience the full velocity spectrum, and second, if the ensemble of particles is large enough to contain the full velocity statistics. The stationary s- and t-Lagrangian ensemble statistics are defined by

$$P(v) = \lim_{V_0 \to \infty} \frac{1}{V_0} \int_{\Omega_0} \frac{v_0(\mathbf{a})}{\langle v_0(\mathbf{a}) \rangle} \delta[v - v_s(s, \mathbf{a})] \mathrm{d}\mathbf{a}, \tag{14}$$

$$\hat{P}(v) = \lim_{V_0 \to \infty} \frac{1}{V_0} \int_{\Omega_0} \delta[v - v_t(t, \mathbf{a})] \mathrm{d}\mathbf{a}, \tag{15}$$

respectively. In practice, the initial volume V_0 is of course finite. In order to achive ergodicity, it needs to be chosen large enough to contain the significant velocity statitics; see also Appendix A. Thus, ergodicity can be expressed as

$$P(v) = \lim_{L \to \infty} \mathcal{P}(v, L, \mathbf{a}) \equiv \mathcal{P}(v), \qquad \hat{P}(v) = \lim_{T \to \infty} \hat{\mathcal{P}}(v, T, \mathbf{a}) \equiv \hat{\mathcal{P}}(v). \tag{16}$$

Under ergodic conditions, the flux-weighting relation (12) implies for the stationary ensemble statistics

$$P(v) = \frac{v}{\langle v_e \rangle} \hat{P}(v), \tag{17}$$

where $\langle v_e \rangle$ is the mean Eulerian velocity magnitude. We now consider the relation between the Lagrangian PDFs and the Eulerian velocity PDF sampled over an infinite domain

$$P_e(v) = \int \delta[v - v_e(\mathbf{x})] \mathrm{d}\mathbf{x}. \tag{18}$$
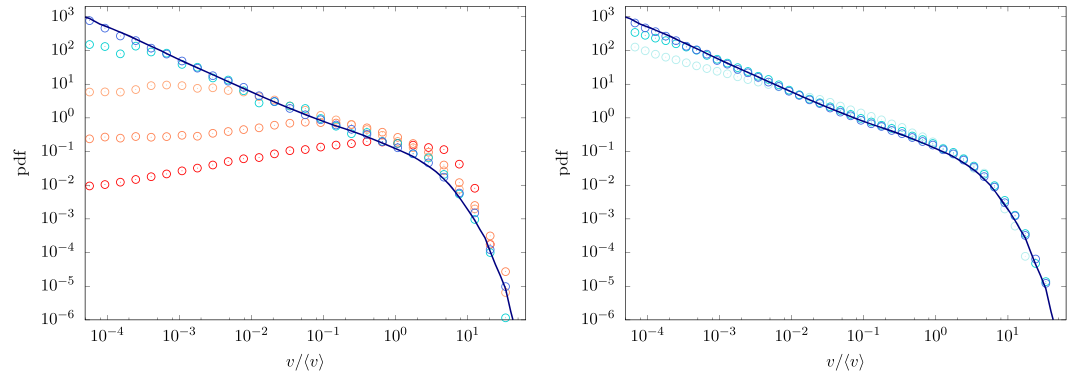
Figure 6. (left panel) Temporal evolution of the ensemble t-Lagrangian PDF $\hat{P}(v, t)$ from the flux-weighted initial particle distribution $p_0(v)$ (red open circles) to the steady t-Lagrangian PDF $\hat{P}(v)$ (navy blue solid line) at times $t = 0, 5, 50, 500, 10^4 \, \tau_c$. (right panel) Temporal evolution of the ensemble t-Lagrangian PDF $\hat{P}(v, t)$ from the uniform initial particle distribution $p_0(v)$ (light blue open circles) to the steady t-Lagrangian PDF $\hat{P}(v)$ (navy blue solid line) at times $t = 0, 10^3, 10^4 \, \tau_c$. The results were computed using 10^6 particles. PDF = probability density function.

The stationary Lagrangian PDF $\hat{P}(v) = P_e(v)$ because of volume conservation as discussed in section B2. Thus, expression (17) implies for the stationary s-Lagrangian PDF

$$P(v) = \frac{v}{\langle v_e \rangle} P_e(v). \tag{19}$$

This is a key relationship for the prediction of particle velocity statistics because the Eulerian velocity PDF can be determined independently from transport.

A detailed discussion on the relations between s-Lagrangian and t-Lagrangian statistics for finite sampling domains is given in Appendix A. There it is shown that the Lagrangian statistics for the rock sample under consideration are stationary and ergodic.

3.2. Evolution of the Lagrangian Velocity Statistics and Stationarity

In the previous sections, we have seen that the s-Lagrangian and t-Lagrangian velocity statistics evolve asymptotically to different steady state distributions, which are related through flux weighting according to (A16). In this section, we study in detail the evolution of the respective statistics from uniform and flux-weighted initial conditions. Note that since the Lagrangian and Eulerian quantities are related through equations (A6) and (A14), studying the Lagrangian statistics evolution includes studying the Eulerian statistics evolution. In the following we only refer to Lagrangian distributions.

3.2.1. Evolution of the s-Lagrangian Velocity Statistics

The s-Lagrangian velocity distribution for an arbitrary initial particle distribution $\rho(\mathbf{a})$ is defined by

$$p(v, s) = \int \delta \left[v - v_s(s, \mathbf{a}) \right] \rho(\mathbf{a}) \mathrm{d}\mathbf{a}. \tag{20}$$

The initial velocity distribution is $p_0(v) = p(v, t = 0)$. We consider the uniform and flux-weighted initial particle distributions (3) and (4). For an ergodic injection domain Ω_0, $p_0(v) = P_e(v)$ for the uniform injection and $p_0(v) = P(v)$ is equal to the stationary s-Lagrangian PDF for the flux-weighted injection. While the injection domain here is not large enough to be ergodic, the initial distribution under flux-weighted conditions is close to the stationary s-Lagrangian PDF as shown in Figure 5. Figure 5 shows the evolution of $p(v, s)$ for the uniform and flux-weighted initial particle distributions (3) and (4). The PDF evolves from both initial distributions toward its steady state $P(v)$. For the flux-weighted initial particle distribution, $p_0(v)$ is skewed toward high-velocity values compared to $p_0(v)$ for the uniform injection with a high probability weight at low velocities. For both initial distributions, the steady state $P(v)$ is reached after a distance of $s \approx 7\ell_p$. We note that the high-velocity part of the PDF converges faster to the steady state than the low-velocity part.

3.2.2. Evolution of the t-Lagrangian Velocity Statistics

The t-Lagrangian velocity PDF for an arbitrary initial particle distribution is defined by

$$\hat{p}(v, t) = \int \delta[v - v_t(t, \mathbf{a})] \rho(\mathbf{a}) \mathrm{d}\mathbf{a}. \tag{21}$$

The initial velocity distribution is $\hat{p}_0(v) = \hat{p}(v, t = 0)$, which is identical to the initial s-Lagrangian velocity PDF $p_0(v)$. As in the previous section, we consider the uniform and flux-weighted initial particle distributions (3) and (4). As pointed out there, $p_0(v) = P_e(v)$, the stationary t-Lagrangian PDF under uniform and $p_0(v) = P(v)$ under flux-weighted injection. The uniform initial condition approximates the stationary distribution but is not equal to it because the injection domain is not ergodic (see Figure 6). Figure 6 shows the evolution of $\hat{p}(v, t)$ for the uniform and flux-weighted initial conditions (3) and (4). As expected, $\hat{p}(v, t)$ evolves toward the steady state distribution $\hat{P}(v)$ from both initial distributions. The time for convergence toward the steady state is $t > 10^4 \tau_c$. Since the average time needed to reach the outlet of the sample is on the order of $6\tau_c$ we use the reinjection procedure to keep all particles in the domain. As for the s-Lagrangian statistics, also here, the high-velocity part of $\hat{p}(v, t)$ converges faster than the low-velocity part.

3.3. Synthesis

In summary, we distinguish between s-Lagrangian statistics, which are sampled equidistantly along particle trajectories, and t-Lagrangian statistics, which are sampled isochronously along particle trajectories. Moreover, we distinguish velocity PDFs that are sampled along single streamlines and velocity PDFs that are obtained by sampling from an ensemble of particles, as well as mixed sampling between particles and along streamlines. We find that the streamwise and ensemble sampled statistics eventually converge after a given streamwise travel distance or streamwise travel time. The convergence of streamwise and ensemble statistics to the same steady state distributions indicates that the underlying velocity process is stationary. The steady s- and t-Lagrangian statistics are related by flux-weighting according to (19).

Stationary conditions are achieved for the t-Lagrangian velocity statistics in case of a uniform injection into an ergodic subdomain Ω_0. For the s-Lagrangian statistics this corresponds to a flux-weighted injection. In the case of ergodic conditions, the s- and t-Lagrangian steady state statistics $P(v)$ and $\hat{P}(v)$ can be obtained by volumetric sampling over an ergodic subdomain because of their relations to the Eulerian velocity PDFs (Dentz et al., 2016). In the following, we model the s-Lagrangian velocity series as a stationary and ergodic Markov process in order to capture the evolution of the s-Lagrangian velocity statistics and its dependence on the initial conditions.

4. Markov Model

We model the s-Lagrangian velocity series $v_s(s)$ as a stationary and ergodic Markov process. This means that the process $v_s(s)$ is fully characterized by the velocity transition probability $r(v, s - s'|v')$, which denotes the PDF of $v_s(s)$ given that $v_s(s') = v'$. Both $r(v, s|v')$ and $p(v, s)$ satisfy the Chapman-Kolmogorov equation

$$p(v, s) = \int_0^\infty r(v, s - s'|v')p(v', s')\mathrm{d}v'. \tag{22}$$

The steady state distribution is an Eigenfunction of $r(v, s|v')$,

$$P(v) = \int_0^\infty r(v, s|v')P(v')\mathrm{d}v'. \tag{23}$$

Furthermore, the transition probability converges to the steady state distribution in the limit of $s \gg \ell_p$,

$$\lim_{s \to \infty} r(v, s|v') = P(v). \tag{24}$$

This implies that $\lim_{s \to \infty} p(v, s) = P(v)$, independent of the initial condition $p_0(v)$. Note also that the joint PDF $P(v, s - s', v')$ of v and v' under stationary conditions is given by

$$p(v, s - s', v') = r(v, s - s'|v')P(v'). \tag{25}$$

Note that Gotovac et al. (2009) studied the statistical properties of the inverse Lagrangian velocity $1/v_s(s)$, which is termed slowness. Evolution equations for the PDF of slowness can be deduced from the Markov model for $v_s(s)$ by variable transformation. In the following, we first construct the transition probability empirically from the direct numerical simulations. This is then used to propagate the s-Lagrangian velocity statistics from uniform initial conditions. Second, we use a Markov model based on a Bernoulli process for the persistence of velocities. Third, we employ an Ornstein-Uhlenbeck (OU) process for $v_s(s)$. The simulated results of these Markov models are then compared to the simulation data presented in the previous sections.
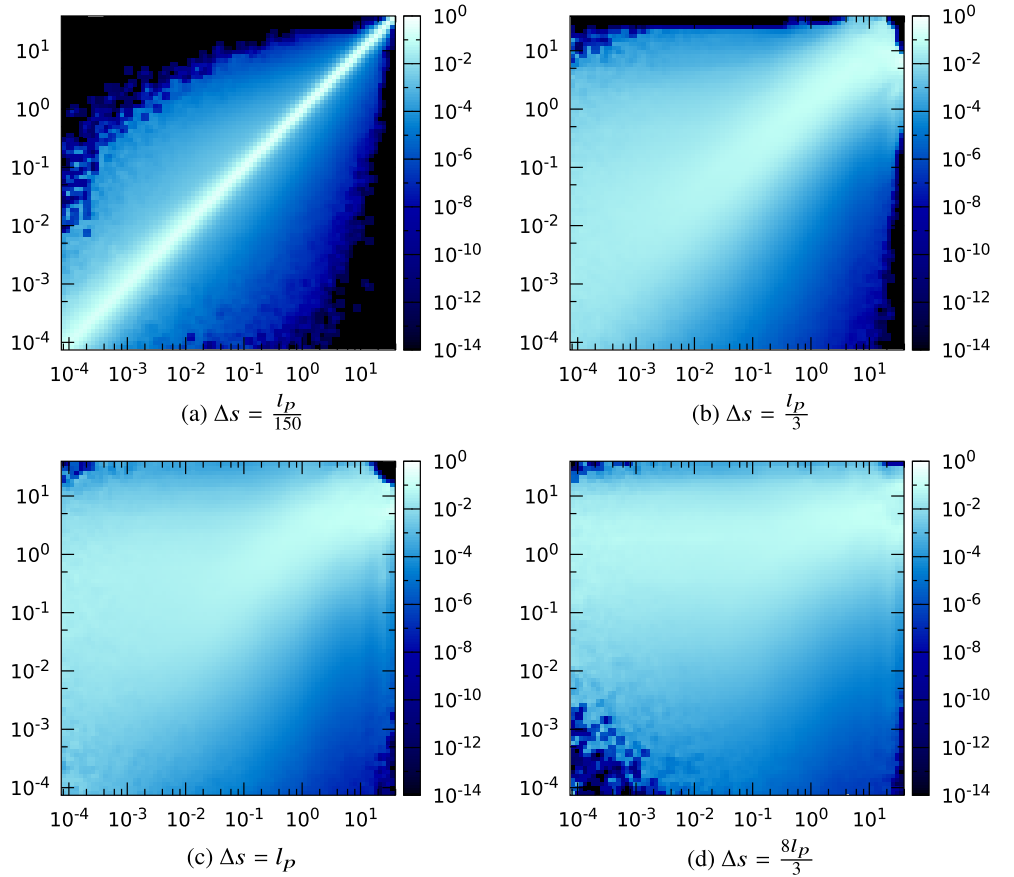
Figure 7. Spatial velocity transition matrices computed with 10^6 particles and respectively with a spatial lag of $\Delta s = \frac{l_p}{150}$, $\Delta s = \frac{l_p}{3}$, $\Delta s = l_p$, and $\Delta s = \frac{8l_p}{3}$ (upper left to lower right).

4.1. Empirical Transition Probability

In this section, we use empirically computed transition probabilities for the modeling of velocity series in space. This approach is conceptually similar to the work of Benke and Painter (2003) and Painter and Cvetkovic (2005) for fractured rock. In order to determine the velocity transition probability $r(v, s - s'|v')$, we discretize the velocity interval $[v_\ell, v_u]$ between minimum and maximum velocities v_ℓ and v_u sampled in the domain into n bins of width $\Delta v_i = v_{i+1} - v_i$, where $v_\ell = v_1$ and $v_u = v_n$ such that

$$v_j = v_1 + \sum_{i=1}^{j-1} \Delta v_j. \tag{26}$$

The empirical transition probability is given by mixed streamwise and ensemble sampling as

$$T_{ij}(\Delta s) = \frac{1}{V_0} \int_{\Omega_0} \frac{1}{L} \int_0^L \mathbb{I}(v_j \leq v(s'' + \Delta s, \mathbf{a}) < v_j + \Delta v_j)|_{v_i \leq v(s'', \mathbf{a}) < v_i + \Delta v_i} \rho(\mathbf{a}) \mathrm{d}s'' \mathrm{d}\mathbf{a}, \tag{27}$$

where $\mathbb{I}(\cdot)$ is 1 if its argument is true and 0 otherwise, and $\Delta s = s - s'$. The empirical transition probability and the conditional probability density $r(v, s - s'|v')$ are related in terms of the stationary joint PDF (25) as

$$T_{ij}(\Delta s) = \int_{v_j}^{v_j + \Delta v_j} \int_{v_i}^{v_i + \Delta v_i} p(v, \Delta s, v') \mathrm{d}v \mathrm{d}v' \Big/ \int_{v_i}^{v_i + \Delta v_i} P(v') \mathrm{d}v'. \tag{28}$$

Note that the empirical determination of the transition probability requires stationary initial conditions. As the initial velocity distribution $p_0(v)$ here is not stationary, as discussed in the previous section, sampling should start once stationary conditions are achieved at approximately $s = 7\ell_p$ (see Figure A1). In practice, mixed sampling along the trajectories of lengths $s \gg \ell_p$ guarantees stationary conditions.
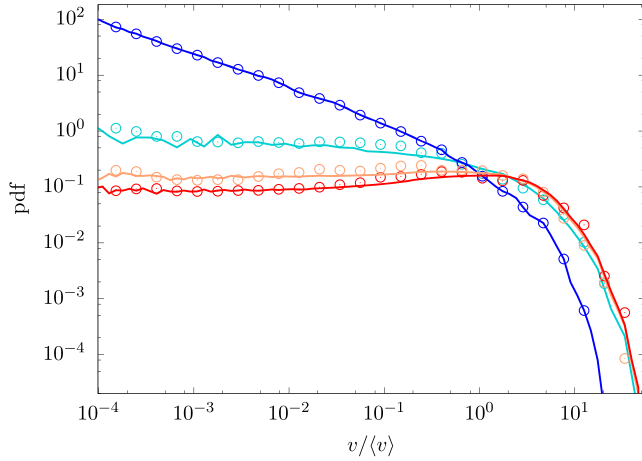
Figure 8. Evolution of the ensemble spatial Lagrangian velocity PDF $P(v, s)$ for direct particle tracking (open circles) and Markov model (solid lines) simulations from the uniform initial particle distribution $p_0(v)$ (blue) to the steady s-Lagrangian PDF $P(v)$ (red) at distances $s = 0, 8/3, 16/3, 8\,\ell_p$. The results were respectively computed with 10^7 and 10^8 particles for the direct simulation and the model. PDF = probability density function.

Figure 7 shows the transition matrix $T_{ij}(\Delta s)$ computed using 10^6 particle trajectories for different lags Δs, and $n = 100$ logarithmically spaced velocity bins such that $v_{i+1} = v_i \exp(1/n)$. The smaller the Δs, the higher the correlation and the more diagonal is the matrix. In principle, any Δs would provide a good estimate for the transition matrix $T_{ij}(\Delta s)$ if the velocity correlation were exponential because in this case, the slope of the correlation function would equal its value everywhere and it could be uniquely characterized by the correlation length ℓ_p. This is not the case here. Figure 3 shows that the correlation function drops for small distances $\Delta s \ll \ell_p$ faster than for larger distances. This means that for small Δs an exponential fit simulates a shorter correlation length than the actual full correlation function. This implies that a transition matrix determined at short Δs sees only this sharp drop and thus underestimates the true correlation. The lag distance Δs needs to be large enough such that the correlation information can be sampled. This means here $\Delta s \geq \ell_p$. For estimating the evolution of the s-Lagrangian statistics we choose $\Delta s = 8\ell_p/3$.

Figure 8 compares the predictions of the velocity Markov model with the data from the direct numerical simulations for the uniform injection mode. The Markov model based on the empirical transition matrix $T_{ij}(\Delta s)$ reproduces the full evolution of the s-Lagrangian velocity statistics $p(v, s)$, which reaches the steady state distribution after the same distance as the data form the direct numerical simulations. Thus, the evolution of the s-Lagrangian velocities can be well represented as a Markov process. In the following section, we consider a Bernoulli process as a Markov relaxation model for this evolution.

4.2. Bernoulli Process

We model the evolution of the Lagrangian velocity $v_s(s)$ by a Bernoulli process such that after each step of length Δs the velocity either remains the same as at the previous step with probability $p_B(\Delta s) = \exp(-\Delta s/\ell_c)$ or changes randomly with probability $1 - p_B(\Delta s)$ according to the steady state PDF $P(v)$. The characteristic length scale ℓ_c of velocity changes is determined below. The transition probability $r(v, \Delta s | v')$ is given explicitly by Dentz et al. (2016)

$$r(v, \Delta s | v') = \exp(-\Delta s/\ell_c)\delta(v - v') + [1 - \exp(-\Delta s/\ell_c)]P(v). \tag{29}$$

Inserting the latter into the Chapman-Kolmogorov equation (22) gives

$$p(v, s + \Delta s) = \exp(-\Delta s/\ell_c)p(v, s) + [1 - \exp(-\Delta s/\ell_c)]P(v)\int_0^\infty p(v', s)\mathrm{d}v'. \tag{30}$$

In the limit $\Delta s \to 0$, we obtain the evolution equation (Dentz et al., 2016)

$$\frac{\partial p(v, s)}{\partial s} = -\frac{1}{\ell_c}\left[p(v, s) - P(v)\right], \tag{31}$$

whose solution for the initial condition $p_0(v)$ is

$$p(v, s) = P(v) + \exp(-s/\ell_c)\left[p_0(v) - P(v)\right]. \tag{32}$$

Thus, we obtain for the mean velocity $\langle v_s(s)\rangle$, the explicit analytical expression

$$\langle v_s(s)\rangle = (\langle v_0\rangle - \langle v_s\rangle)\exp(-s/\ell_c) + \langle v_s\rangle, \tag{33}$$

where $\langle v_0\rangle$ is the average initial velocity and $\langle v_s\rangle$ the average s-Lagrangian steady state velocity. We use this expression to estimate the characteristic length scale from the direct numerical simulations as shown in Figure 9. We find $\ell_c = 2.5\ell_p$, which is of the order or the pore length.

Figure 10 compares the evolution of $p(v, s)$ obtained from the direct numerical simulations with the prediction (32) of the Bernoulli model for uniform injection conditions. The Bernoulli model converges to the
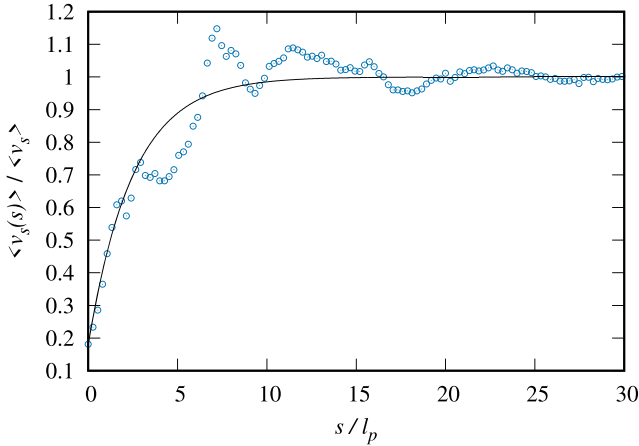
Figure 9. Evolution of the mean s-Lagrangian velocity $\langle v_s(s) \rangle$ (circles) for a uniform initial distribution and expression (33) (solid line) with $\ell_c = 2.5\ell_p$.

steady state distribution after $s \approx 3\ell_c$ but does not reproduce the velocity PDFs at intermediate distances. Note that the Bernoulli model uses the same convergence rate ℓ_c^{-1} for all velocities. While this model represents the evolution of the high-velocity part of $p(v,s)$ relatively well, the low-velocity part evolves faster than the data from the direct numerical simulations. This indicates that the convergence rate may be velocity dependent. In the next section, we model this behavior with an alternative Markov model for $v_s(s)$.

4.3. OU Process

In this section, we consider a velocity Markov model for the evolution of $v_s(s)$ that is based on the OU process (Gardiner, 2010; Morales et al., 2017),

$$\frac{\mathrm{d}w(s)}{\mathrm{d}s} = -\ell_c^{-1}w(s) + \sqrt{2\ell_c^{-1}}\xi(s), \tag{34}$$

where $\xi(s)$ is a Gaussian white noise characterized by zero mean, $\langle \xi(t) \rangle = 0$ and covariance $\langle \xi(s)\xi(s') \rangle = \delta(s - s')$. The angular brackets denote the noise average over all realizations of $\xi(s)$. The OU process has originally been considered for the modeling of the stochastic (in time) velocity fluctuations of Brownian particles (Langevin, 1908; Risken, 1996; Uhlenbeck & Ornstein, 1930), later also for particle velocities in turbulent flows (Pope, 2000). From a mathematical point of view, the OU model is a stationary Gaussian Markov process. Its increments are Gaussian random variables. Its distribution $\phi(w,s)$ satisfies the Fokker-Planck equation (Risken, 1996)

$$\frac{\partial \phi(w,s)}{\partial s} - \ell_c^{-1}\frac{\partial w\phi(w,s)}{\partial w} - \ell_c^{-1}\frac{\partial^2 \phi(w,s)}{\partial w^2} = 0. \tag{35}$$

It relaxes from any initial distribution $\phi_0(w)$ to a Gaussian steady state distribution $\phi(w)$, which has zero mean and unit variance for the specific process (34). We use this process here to model the stochastic evolution of the particle velocity $v_s(s)$ and the relaxation of its statistics from any initial distribution $p_0(v)$ toward the steady state $P(v)$. This requires to map $v_s(s)$ onto $w(s)$ through their steady state PDFs. This is done through the Smirnov transform (Devroye, 1986)

$$w(s) = \Phi^{-1}(\Pi[v_s(s)]) \equiv \mathcal{M}[v_s(s)], \qquad v_s(s) = \Pi^{-1}(\Phi[w(s)]), \tag{36}$$

where $\Pi(v)$ and $\Phi(w)$ are the cumulative distributions of $v(s)$ and $w(s)$,

$$\Pi(v) = \int_0^v P(v')\mathrm{d}v', \qquad \Phi(w) = \int_{-\infty}^w \phi(w')\mathrm{d}w'. \tag{37}$$

The latter is given by $\Phi(w) = [1+\mathrm{erf}(w/\sqrt{2})]/2$. As $\phi(s)$ is a unit Gaussian, this map generates $w(s)$ as the normal score of $v_s(s)$. This map guarantees that $p(v,s)$ evolves from any initial distribution $p_0(v)$ toward its steady state $P(v)$ on the relaxation scale ℓ_c, which is set equal to the one determined for the Bernoulli model in the previous section. Note that all the normal scores $w(s)$ evolve with the same rate ℓ_c^{-1}. Note that the transition probability $r_w(w, \Delta s|w')$ is given by the Gaussian distribution (Risken, 1996)

Figure 10. Evolution of the ensemble spatial Lagrangian velocity PDF $P(v,s)$ for both direct particle tracking (open circles) and Bernoulli process (solid lines) simulations from the uniform initial particle distribution $p_0(v)$ (blue) to the steady s-Lagrangian PDF $P(v)$ (red) for distance $s = 0, 8/3, 10 \ell_p$. The results were respectively computed with 10^7 and $5 \cdot 10^8$ particles for the direct simulation and the model. PDF = probability density function.

$$r_w(w, \Delta s|w') = \frac{\exp\left(-\frac{[w-w'\exp(-\Delta s/\ell_c)]^2}{2[1-\exp(-2\Delta s/\ell_c)]}\right)}{\sqrt{2\pi\left[1-\exp(-2\Delta s/\ell_c)\right]}}. \tag{38}$$

The transition probability for the velocity process $r(v, \Delta s|v')$ is given in terms of $r_w(w, \Delta s|w')$ according to the map (36)

$$r(v, \Delta s|v') = r_w[\mathcal{M}(v), \Delta s|\mathcal{M}(v')]\frac{\mathrm{d}\mathcal{M}(v)}{\mathrm{d}v}, \tag{39}$$

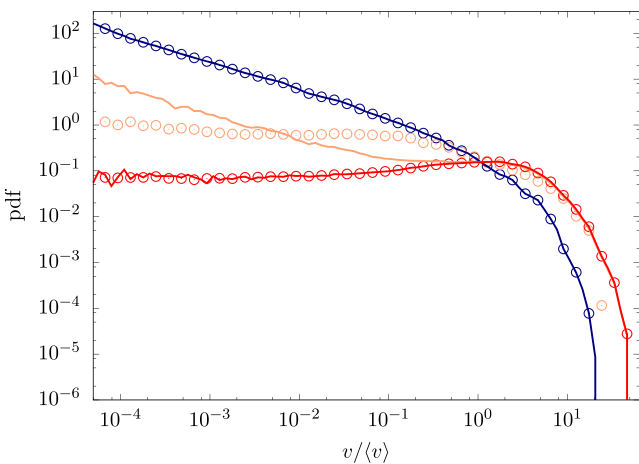which in general leads to velocity-dependent convergence rates for $p(v,s)$.
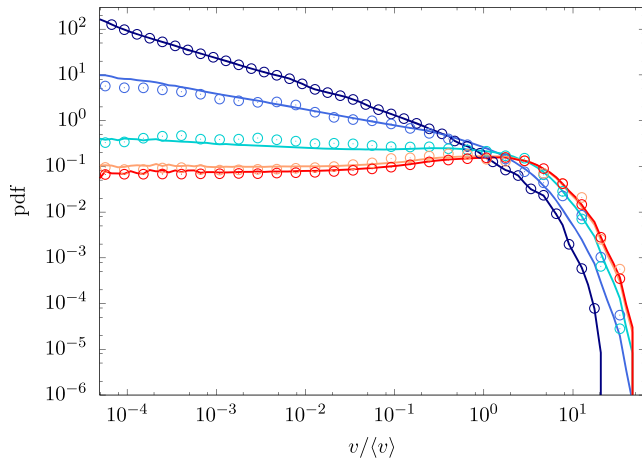
Figure 11. Evolution of the ensemble spatial Lagrangian velocity PDF $P(v, s)$ for direct particle tracking (open circles) and Ornstein-Uhlenbeck process (solid lines) simulations from the uniform initial particle distribution $p_0(v)$ (blue) to the steady s-Lagrangian PDF $P(v)$ (red) at distance $s = 0, 4/3, 4, 8, 10 \, \ell_p$. The results were respectively computed with 10^7 and $5 \cdot 10^8$ particles for the direct simulation and the model. PDF = probability density function.

The process (34) is solved for an ensemble of particles. The initial values $w(s = 0) = w_0$ are obtained from $v_s(s = 0) = v_0$ by the map (36) as $w_0 = \Phi^{-1}[\Pi(v_0)]$, where the v_0 are distributed according to $p_0(v)$. Once w_0 is obtained, the process (34) is solved numerically using an explicit Euler scheme,

$$w_{n+1} = w_n - \ell_c^{-1} w_n \Delta s + \sqrt{2\ell_c^{-1} \Delta s} \xi_n, \tag{40}$$

where $w_n = w(n\Delta s)$ and ξ_n is a Gaussian random variable with 0 mean and unit variance. The value w_{n+1} is transformed back to the velocity $v_s(n\Delta s)$ via equation (36) at every step. The discretization of scheme (40) is chosen such that $\Delta s \le \ell_c/10$.

Figure 11 compares the results of the velocity Markov model based on the OU process with the data from the direct numerical simulations. The Markov model is capable of predicting the evolution of $p(v, s)$ in every aspect at small, intermediate and large distances from the inlet. The velocity dependence of convergence rates in the OU-based Markov model for $v_s(s)$ accurately captures the evolution of $p(v, s)$ for all velocity classes.

4.4. Synthesis

In summary, based on the stationary and ergodic properties of the s-Lagrangian velocity series, we model their stochastic dynamics as an ergodic Markov chain. We consider three different Markov models. First is a Markov model based on an empirical transition probability, which is obtained from conditional equidistant velocity sampling along streamlines. This model naturally reproduces the evolution of the s-Lagrangian velocity PDF and confirms the Markovian nature of the velocity transitions. Second, we consider a Bernoulli velocity model, which at each step either persists at the velocity of the previous step or changes to a new velocity, which is randomly sampled from the stationary s-Lagrangian PDF. This model yields an evolution of the s-Lagrangian PDF from an initial to the stationary PDF. However, it uses the same convergence rate for all velocity classes, which does not capture the evolution at small velocities. Third, we consider a velocity transition model that is based on an OU process for the normal scores of the s-Lagrangian velocities. This process correctly predicts the full evolution of the s-Lagrangian velocity PDF and is parameterized by the stationary Lagrangian velocity PDF and a characteristic relaxation scale ℓ_c. The former is related to the Eulerian velocity PDF, a flow attribute; the latter is of the order of the characteristic pore length. Thus, this stochastic velocity model can be parameterized in terms of hydraulic and geometric characteristics of the porous medium.

5. Conclusions

We have presented a comprehensive analysis of Lagrangian pore-scale velocity series. Even though the study is based on velocity data in the three-dimensional pore structure obtained from X-ray microtomography of a Berea sandstone sample, the presented methods and results are valid for particle motion in steady pore-scale flows in general. Our analysis has revealed the stochastic dynamics of particle velocities and led to the formulation of a predictive modeling approach for the velocity evolution based on Markov processes for the streamwise Lagrangian velocities. These results are part of the endeavor of setting up an upscaling framework for hydrodynamic flow and transport from the pore to the Darcy scale. The past years have seen a significant increase of experimental and numerical pore-scale studies along with improved imaging techniques and computational resources. The presented methods for the statistical analysis of pore-scale velocity data provide new tools for the interpretation of such experimental and numerical data and their use in the upscaling of flow and transport.

The evolution of the velocity statistics represents a key feature that needs to be accounted for both in the interpretation of experimental and numerical velocity data and in the modeling and upscaling of particle transport. For example, in particle tracking and particle imaging velocimetry, the measured velocity distributions may be dependent on the initial preparation (this means on the seeding of the injection volume with particles) and not be representative of the porous sample. Furthermore, data analysis often invokes stationarity of the measured particle velocities, which in general, however, is not the case and depends again on

the injection condition. Pore-scale velocity variability is at the origin of hydrodynamic dispersion and other transport phenomena observed on the Darcy scale. The Kubo formula provides a measure for hydrodynamic dispersion in terms of the time integral of the t-Lagrangian velocity covariance,

$$\mathcal{D}(t) = \int\limits_0^t \langle v_t'(t')v_t'(t)\rangle \mathrm{d}t',$$
(41)

where $v_t'(t)$ denotes the fluctuation of the t-Lagrangian velocity around its mean. Dispersion in general evolves in time and depends on the initial conditions (stationary or nonstationary) and the time evolution of the velocity statistics. For example, dispersion at times smaller than the advection time τ_v is ballistic and given by $\mathcal{D}(t) = \sigma_0^2 t$ where σ_0^2 is the variance of the PDF of initial velocities $p_0(v)$, which clearly depends on the initial velocity distribution. The asymptotic behavior is determined by the velocity correlation time and velocity variance, which are related to the intermittent temporal velocity signals. The tailing of particle breakthrough curves is determined by the occurrence of low velocities and their spatial persistence. Thus, the retention phenomena also depends on the evolution of the velocity statistics and the initial preparation of the system. For example, a uniform initial particle distribution emphasizes more the low end of the velocity spectrum than a flux-weighted. Thus, the corresponding breakthrough curves, or residence time distributions in a sample, may be significantly different depending on the initial conditions.

These behaviors as they evolve in time hold a certain complexity, which is reflected in the intermittent features of Lagrangian velocity time series. This complexity can be removed by applying a different sampling protocol, namely, by sampling equidistantly along particle trajectories. This streamwise spatial point of view provides a significant simplification of otherwise complex phenomena and thus opens new possibilities for transport modeling and upscaling. The formulation of the s-Lagrangian velocity magnitude as an ergodic Markov chain renders particle motion naturally as a (correlated) continuous time random walk (Berkowitz et al., 2006; Dentz et al., 2016; Le Borgne et al., 2008) or time-domain random walk (Benke & Painter, 2003; Painter & Cvetkovic, 2005), because streamwise particle motion can be modeled in terms of fixed spatial steps Δs, which take the random time $\tau = \Delta s/v_s$.

$$s_{n+1} = s_n + \Delta s, t_{n+1} = t_n + \tau_n.$$
(42)

The Markov property of the s-Lagrangian velocity is transferred to the transition times τ whose distribution evolves in time just like the s-Lagrangian velocity PDF. CTRW formulations that are based on a single transition time distribution $\psi(t)$ are not able to model the impact of nonstationary initial conditions from the s-Lagrangian point of view, or stationary initial conditions from a t-Lagrangian point of view. Note that the process (42) describes particle motion along a tortuous streamline. The motion in three-dimensional Cartesian coordinates can be obtained either by an additional characterization of the direction vector $\omega(s, \mathbf{a}) = \mathbf{v}[\mathbf{x}(s, \mathbf{a})]/v_e[\mathbf{x}(s, \mathbf{a})]$ in equation (6) as a stochastic process, or the projection of the streamwise motion on the mean flow direction in terms of the advective tortuosity (Koponen et al., 1996; Dentz et al., 2018).

The OU process for the normal scores of the s-Lagrangian velocities correctly predicts the full evolution of the s-Lagrangian velocity PDF and is parameterized by the stationary Lagrangian velocity PDF and the characteristic correlation scale. The former is related to the Eulerian velocity PDF, a flow attribute; the latter is of the order of the characteristic pore length. This stochastic velocity model can be parameterized in terms of hydraulic and geometric characteristics of the porous medium. Thus, it is a predictive model in the sense that it can be based on the characterization of transport independent quantities, which is an important step for flow and transport upscaling from the pore to the Darcy scale. While significant progress has been made (Alim et al., 2017; De Anna et al., 2017; Dentz et al., 2018), the relation between pore structure and pore velocity distribution still remains an open issue. In addition to the OU velocity model, we consider a Bernoulli process, which reproduces the velocity evolution qualitatively but lacks the correct convergence rates for low and intermediate velocities. Yet, due to its simplicity, it may serve to obtain fast qualitative estimates of transport features related to the evolution of particle velocity statistics. Finally, note that the methodology used here applies to transport in steady flow through heterogeneous media in general, for which a relaxation of the Lagrangian velocity statistics toward a steady state can be observed such as Darcy-scale fractured and porous media (Cvetkovic et al., 1996; Dentz et al., 2016; Kang et al., 2017; Le Borgne et al., 2007).

We consider here purely advective particle motion and do not account for the effect of diffusion on particle motion. Thus, the derived stochastic framework is directly relevant for advection-dominated pore-scale transport. In fact, practically relevant pore-scale Peclet numbers may range from 10^{-2} to 10^6 (Bear, 1972; Bijeljic & Blunt, 2006). In the presented Markov models, velocity transitions occur essentially with a fixed spatial frequency which is given by the inverse velocity correlation length. In the presence of diffusion, velocity transitions can also occur due to particle transitions between streamlines, a process that is related to a constant frequency in time, namely, the inverse diffusion time over the characteristic velocity length scale. Advective and diffusive velocity transitions may depend on a local Péclet number. Thus, the derived Markov model provides a basis to account for the impact of velocity variability and diffusion on hydrodynamic dispersion. Furthermore, pore-scale flow variability has an impact on processes such as the filtration of colloidal particles and bacteria (Liang et al., 2018) as well as mixing between dissolved chemicals (Kree & Villermaux, 2017), while these processes are also affected by other factors such as volume exclusion and interactions with the solid matrix as well as diffusion; for example, the derived stochastic model for Lagrangian particle velocities may serve as a starting point to account systematically for the effect of hydrodynamic variability.

In summary, the fact that the Lagrangian velocity statistics are stationary allows for the stochastic description of the s-Lagrangian velocity dynamics as an ergodic Markov chain. This stochastic framework renders particle motion as a correlated continuous time random walk. The consequences of the stochastic s-Lagrangian velocity dynamics for the prediction of preasymptotic spatial and temporal transport characteristics and their systematic upscaling are studied elsewhere.

Appendix A: Equidistant and Isochronous Ensemble Statistics

In this section, we discuss the relations between the s- and t-Lagrangian ensemble statistics for finite sampling domains.

A1. Equidistant Sampling: s-Lagrangian Statistics

The ensemble s-Lagrangian velocity PDF is obtained by sampling the velocity magnitude $v_s(s, \mathbf{a})$ at a given streamline distance s in the flux-weighted ensemble of particles comprised in the injection domain Ω_0

$$P(v, s) = \frac{1}{V_0} \int_{\Omega_0} \frac{v_0(\mathbf{a})}{\langle v_0(\mathbf{a}) \rangle} \delta[v - v_s(s, \mathbf{a})] d\mathbf{a}, \tag{A1}$$

each particle being weighted by its initial velocity. This PDF can be computed for any distance $s \geq 0$ and in general evolves with distance. The mixed s-Lagrangian PDF is defined by sampling along streamlines and between particles as

$$P_m(v, L) = \frac{1}{L} \int_0^L \frac{1}{V_0} \int_{\Omega_0} \frac{v(\mathbf{a})}{\langle v(\mathbf{a}) \rangle} \delta[v - v_s(s, \mathbf{a})] d\mathbf{a} ds. \tag{A2}$$

This method samples more statistics than its ensemble and streamwise counterparts since it integrates over all particles labeled by $\mathbf{a}$ and distances s traveled. Under ergodic conditions, sampling along streamlines and ensemble sampling are equivalent. As discussed in the main text, this can be achieved for sampling distances L and initial volumes V_0 large enough that a representative part of the velocity variability can be experienced. Under these conditions, the streamwise, ensemble and mixed s-Lagrangian PDFs are identical and independent of L and $\mathbf{a}$ (streamwise) and s (ensemble),

$$\mathcal{P}(v) = P(v) = P_m(v). \tag{A3}$$

Figure A1 shows the streamwise, ensemble and mixed s-Lagrangian PDFs for $L \approx 10^8 \ell_c$ in the streamwise case and $s = 7\ell_c$ for the ensemble. The three different PDFs are in very good agreement, which implies that the reinjection method detailed in section 2.2.2 is ergodic (convergence of the streamwise PDF), and that stationary conditions are already attained within the sample size (convergence of the ensemble PDF). The evolution of the ensemble s-Lagrangian PDF is analyzed in detail in section 3.2. As the different statistics are identical in steady state, we refer to the steady state distribution as $P(v)$.
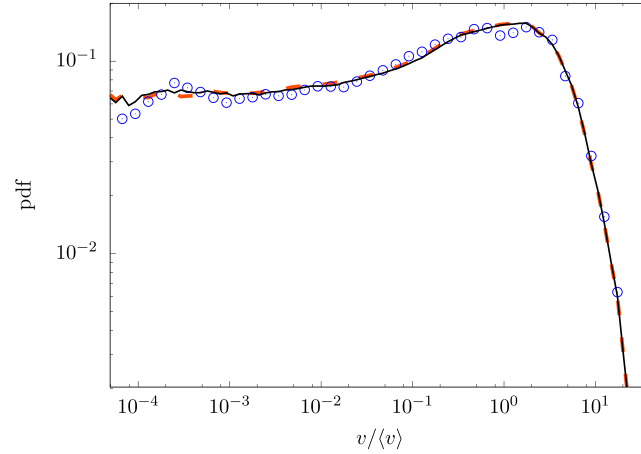
Figure A1. Comparison between the streamwise $\mathcal{P}(v)$ (orange dashed line), ensemble $P(v)$ (blue circles, computed with 10^7 particles), and mixed $P_m(v)$ (solid black line, computed with 10^5 particles) of the s-Lagrangian velocity PDFs. PDF = probability density function.

A2. Equidistant Sampling: s-Eulerian Statistics

The fluid flow map φ_s, defined as

$$\varphi_s : \mathbf{a} \mapsto \mathbf{x}(s, \mathbf{a}) \tag{A4}$$

maps the initial particle position $\mathbf{a}$ on the particle position $\mathbf{x}(s, \mathbf{a})$ at distance s according to (6). The s-Eulerian velocity PDF is obtained by volumetric sampling of the Eulerian velocity magnitude $v_e(\mathbf{x})$ in the subdomain $\Omega(s) = \varphi_s(\Omega_0) \subset \Omega_f$, where Ω_f is the flow domain,

$$P_e(v, s) = \frac{1}{V(s)} \int_{\Omega(s)} \delta[v - v_e(\mathbf{x})] \mathrm{d}\mathbf{x}. \tag{A5}$$

The relation between the s-Eulerian velocity PDF $P_e(v, s)$ and the ensemble s-Lagrangian velocity PDF $P(v, s)$ is obtained by using the map (A4) in order to transform the integration variable $\mathbf{a} \to \mathbf{x}$ in (A1). Note that the map (A4) is not volume preserving. Thus, $V(s) \neq V(t)$. In section B1 we show that

$$P(v, s) = \frac{v}{\mu_e(s)} P_e(v, s), \tag{A6}$$

with the s-Eulerian mean velocity $\mu_e(s)$. Equation (A6) means that the s-Lagrangian and s-Eulerian velocity PDFs are related through flux weighting. The s-Eulerian mean velocity $\mu_e(s)$ is

$$\mu_e(s) = \int_0^\infty P_e(v, s) \mathrm{d}v, \tag{A7}$$

which in general evolves with distance s. Under ergodic conditions, the s-Eulerian PDF is stationary and thus independent from s, $P_e(v, s) = P_e(v)$ and $\mu_e(s) = \langle v_e \rangle$. The Lagrangian and Eulerian statistics are related by

$$P(v) = \frac{v}{\langle v_e \rangle} P_e(v). \tag{A8}$$

A3. Isochronous Sampling: t-Lagrangian Statistics

Sampling of the velocity magnitude $v_t(t, \mathbf{a})$ between particles gives the ensemble t-Lagrangian PDF

$$\hat{P}(v, t) = \frac{1}{V_0} \int_{\Omega_0} \delta[v - v_t(t, \mathbf{a})] \mathrm{d}\mathbf{a}, \tag{A9}$$

where Ω_0 is the fluid domain in which particles are initially placed, and V_0 is its volume. The mixed t-Lagrangian PDF samples velocity magnitudes both between particles and along particle trajectories

$$\hat{P}_m(v, T) = \frac{1}{V_0} \int_{\Omega_0} \frac{1}{T} \int_0^T \delta[v - v_t(t, \mathbf{a})] \mathrm{d}t \mathrm{d}\mathbf{a}. \tag{A10}$$
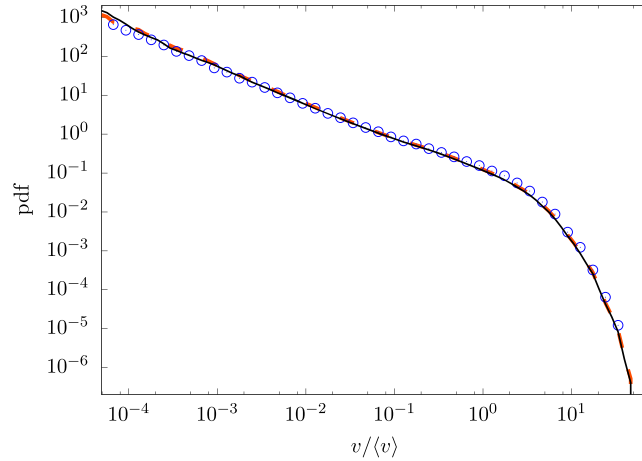
Figure A2. Comparison of the streamwise $\hat{\mathcal{P}}(v)$ (orange dashed line), ensemble $\hat{P}(v)$ (blue circles, computed with 10^6 particles), and mixed $\hat{P}_m(v)$ (solid black line, computed with 10^4 particles) of the t-Lagrangian velocity PDFs. PDF = probability density function.

The mixed method is often used for the empirical determination of velocity statistics from particle tracking velocimetry because it yields better statistics than either sampling along a single trajectory or between particles. Under ergodic conditions, the sampling of the velocity magnitude along a streamline for a long enough time T is identical to ensemble sampling for a large enough time t. The sampling time T and initial domain Ω_0 need to be large enough such that the sampled velocity variability is representative. Under these conditions, $\hat{\mathcal{P}}(v, T, \mathbf{a}) = \hat{\mathcal{P}}(v)$ is independent of $\mathbf{a}$ and T and $\hat{P}(v, t) = \hat{P}(v)$ is independent of the sampling time t such that

$$\hat{\mathcal{P}}(v) = \hat{P}(v) = \hat{P}_m(v). \tag{A11}$$

Figure A2 shows $\hat{\mathcal{P}}(v, T, \mathbf{a})$, $\hat{P}(v, t, V_0)$, and $\hat{P}_m(v, T, V_0)$. The three statistics are in good agreement, which indicates that in the numerical simulations, ergodic conditions are reached.

A4. Isochronous Sampling: t-Eulerian Statistics

The fluid flow map

$$\varphi_t : \mathbf{a} \mapsto \mathbf{x}(t, \mathbf{a}) \tag{A12}$$

maps the initial particle position $\mathbf{a}$ on the position $\mathbf{x}(t, \mathbf{a})$ at time t. The t-Eulerian velocity PDF corresponding to $\hat{P}_t(v, t)$ is obtained by volumetric sampling of the Eulerian velocity magnitude $v_e(\mathbf{x})$ in the subdomain $\hat{\Omega}(t) = \varphi_t(\Omega_0)$,

$$\hat{P}_e(v, t) = \frac{1}{V_0} \int_{\hat{\Omega}(t)} \delta\left[v - v_e(\mathbf{x})\right] \mathrm{d}\mathbf{x}. \tag{A13}$$

Note that $\hat{\Omega}(t)$ is the domain occupied by the particles after time t. Its volume $\hat{V}(t)$ equals the initial volume $\hat{V}(t) = V_0$ because the map (A12) is volume conserving. The t-Lagrangian PDF $\hat{P}(v, t)$ can be related to the t-Eulerian PDF $\hat{P}_e(v, t)$ by using the map (A12) in (A9) to transform the integration variable from $\mathbf{a} \rightarrow \mathbf{x}$. Thus, we obtain

$$\hat{P}(v, t) \equiv \hat{P}_e(v, t), \tag{A14}$$

see section B2. Note that the Jacobian of the map φ_t is 1, again because $\mathbf{v}(\mathbf{x})$ is volume conserving. Also note that this is a purely kinematic relation, which is true independently of the question whether the system is ergodic or not. Under ergodic conditions, (A11) and (A14) imply that the Eulerian statistics are independent of t, $\hat{P}_e(v, t) = \hat{P}_e(v)$ and

$$\hat{P}_e(v) = \hat{P}(v) = \hat{\mathcal{P}}(v). \tag{A15}$$

In the following, we refer to the steady state distribution as $\hat{P}(v)$ because the three statistics are identical in the steady state.
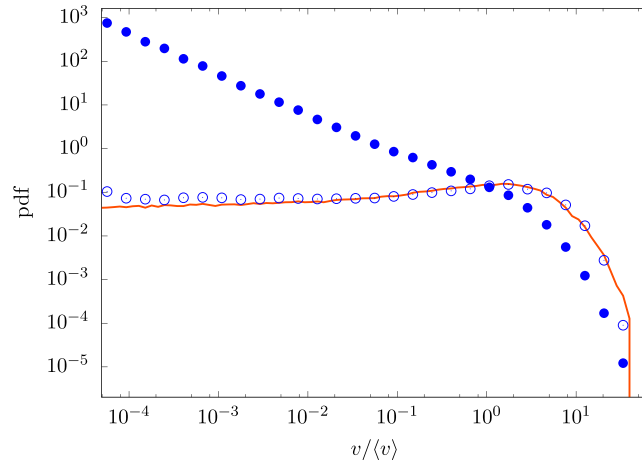
Figure A3. Ensemble t-Lagrangian PDF $\hat{P}(v)$ (full circles, computed with 10^6 particles) and s-Lagrangian PDF $P(v)$ (open circles, computed with 10^7 particles) and the flux-weighting relation (A16) (solid line). PDF = probability density function.

A5. Relations Between Isochronous and Equidistant Statistics

We have seen in (A15) that the statistics of the isochronously sampled Lagrangian velocity $\hat{\mathcal{P}}(v)$ along a trajectory equals the Eulerian velocity statistics $\hat{P}_e(v)$ under ergodic conditions and that the streamwise s- and t- Lagrangian velocity statistics are related through a flux weighted relation (17). Furthermore, under ergodic conditions, we know from (A3) that the ensemble equals the streamwise s-Lagrangian PDF, $P(v) = \mathcal{P}(v)$, and from (A11) that the ensemble is identical to the streamwise t-Lagrangian PDF, $\hat{P}(v) = \hat{\mathcal{P}}(v)$. Thus, we obtain from (17) the following relation

$$P(v) = \frac{v}{\langle v_e \rangle} \hat{P}(v). \tag{A16}$$

Figure A3 compares the ensemble t- and s-Lagrangian statistics at $t = 9 \cdot 10^3 \tau_c$ and $s = 7\ell_p$. Both statistics are in good agreement with respect to relations (17) and (A16), which confirms again that ergodic conditions are attained. Furthermore, note that under ergodic conditions the steady s-Lagrangian PDF $P(v)$ is related to the s-Eulerian PDF by relation (A8), while the steady t-Lagrangian is equal to the t-Eulerian PDF (see (A11)). Thus, the s- and t-Eulerian velocity PDFs are identical under ergodic conditions,

$$P_e(v) = \hat{P}_e(v). \tag{A17}$$

These relations imply that the t-Lagrangian velocity statistics are stationary for the initial distribution $P_e(v)$, which corresponds to a uniform injection over an area or volume that is large enough to be ergodic. The s-Lagrangian statistics are accordingly stationary for a flux-weighted injection over a large enough injection domain.

Furthermore, we have defined s- and t- Eulerian velocity distributions, which correspond to the respective s- and t-Lagrangian statistics. The Eulerian distributions are obtained by volumetric sampling in the sub-volumes $\Omega(s)$ and $\hat{\Omega}(t)$ which are obtained by mapping the injection domain Ω_0 by the respective flow maps φ_s and φ_t. The s-Lagrangian and s-Eulerian velocity PDFs are related by flux-weighting according to (A6); the t-Eulerian and Lagrangian are identical (see (A14)).

Appendix B: Relations Between s- and t-Lagrangian Statistics

In the following, we provide some details on the derivation of the relations between s- and t-Lagrangian statistics reported on in the previous section.

B1. Relation Between the s-Eulerian Velocity PDF $P_e(v, s)$ and the Ensemble s-Lagrangian Velocity PDF $P(v, s)$

We derive the relation between the s-Eulerian velocity PDF $P_e(v)$ and the ensemble s-Lagrangian velocity PDF $P(v, s)$. $P(v, s)$ is defined as

$$P(v, s) = \frac{1}{V_0} \int_{\Omega_0} \frac{v(\mathbf{a})}{\langle v(\mathbf{a}) \rangle} \delta[v - v_s(s, \mathbf{a})] d\mathbf{a}, \tag{B1}$$

which is originally defined on the initial injection domain Ω_0 and is parameterized through flux weighting. V_0 is the volume of Ω_0, and $\mathbf{a}$ is the initial position of particle $\mathbf{a}$. We can derive this definition to any domain $\Omega(s)$, which is the domain occupied by the particles after they have traveled the distance s along their streamline, this is achieved using the map $\mathbf{a} \rightarrow \mathbf{x}(s, \mathbf{a})$. Doing so we obtain

$$P(v, s) = \frac{1}{V_0} \int_{\Omega(s)} \mathbb{J}(s, \mathbf{a})^{-1} \frac{v(\mathbf{a})}{\langle v(\mathbf{a}) \rangle} \delta[v - v_e(\mathbf{x}(s, \mathbf{a}))] d\mathbf{x}, \tag{B2}$$

where $\mathbb{J}(s, \mathbf{a}) = \|d\mathbf{x}(s, \mathbf{a})/d\mathbf{a}\|$ is the Jacobian of the transformation. It can be determined as follows. First, we note that its derivative is given by (Batchelor, 2000, p., 75)

$$\frac{d}{ds} \mathbb{J}(s, \mathbf{a}) = \mathbb{J}(s, \mathbf{a}) \nabla \cdot \left(\frac{\mathbf{v}[\mathbf{x}(s, \mathbf{a})]}{v_s(s, \mathbf{a})} \right), \tag{B3}$$

which can be expanded to

$$\frac{d}{ds} \mathbb{J}(s, \mathbf{a}) = -\mathbb{J}(s, \mathbf{a}) \frac{\mathbf{v}[\mathbf{x}(s, \mathbf{a})] \cdot \nabla v_s(s, \mathbf{a})}{v_s(s, \mathbf{a})^2}, \tag{B4}$$

where we used that $\nabla \cdot \mathbf{v}(\mathbf{x}) = 0$. We obtain for the derivative of $v_s(s, \mathbf{a}) = v_e[\mathbf{x}(s, \mathbf{a})]$ with respect to s,

$$\frac{dv_s(s, \mathbf{a})}{ds} = \frac{\mathbf{v}[\mathbf{x}(s, \mathbf{a})] \cdot \nabla v_s(s, \mathbf{a})}{v_s}, \tag{B5}$$

where we used (6). Thus, equation (B4) reduces to

$$\frac{d}{ds} \mathbb{J}(s, \mathbf{a}) = -\frac{1}{v_s(s, \mathbf{a})} \frac{dv_s(s, \mathbf{a})}{ds} \mathbb{J}(s, \mathbf{a}). \tag{B6}$$

Integrating the differential equation (B6) for the initial condition $\mathbb{J}(s = 0, \mathbf{a}) = 1$ yields

$$\mathbb{J}(\mathbf{a}, s) = \frac{v_e(\mathbf{a})}{v_e[\mathbf{x}(s, \mathbf{a})]}. \tag{B7}$$

Which leads to

$$P(v, s) = \frac{1}{V_0} \int_{\Omega(s)} \frac{v(\mathbf{a})}{\langle v(\mathbf{a}) \rangle} \frac{v(\mathbf{x})}{v(\mathbf{a})} \delta[v - v_e(\mathbf{x}(s, \mathbf{a}))] d\mathbf{x}, \tag{B8}$$

$$P(v, s) = \frac{1}{V_0} \int_{\Omega(s)} \frac{v(\mathbf{x})}{\langle v(\mathbf{a}) \rangle} \delta[v - v_e(\mathbf{x}(s, \mathbf{a}))] d\mathbf{x}, \tag{B9}$$

and because of the Dirac-delta,

$$P(v, s) = \frac{1}{V_0} \frac{v}{\langle v(\mathbf{a}) \rangle} \int_{\Omega(s)} \delta[v - v_e(\mathbf{x}(s, \mathbf{a}))] d\mathbf{x}. \tag{B10}$$

Furthermore, we have $\frac{1}{\langle v(\mathbf{a}) \rangle} = \frac{V_0}{\langle v(\mathbf{x}) \rangle V(s)}$, which can be seen as follows. First, we observe that

$$\int_{\Omega_0} \frac{v(\mathbf{a})}{\langle v(\mathbf{a}) \rangle} d\mathbf{a} = V_0 \tag{B11}$$

by definition. Using the transformation $\mathbf{a} \rightarrow \mathbf{x}(s, \mathbf{a})$, we can obtain

$$\int_{\Omega(s)} \mathbb{J}^{-1} \frac{v(\mathbf{a})}{\langle v(\mathbf{a}) \rangle} d\mathbf{x} = \int_{\Omega(s)} \frac{v(\mathbf{x})}{v(\mathbf{a})} \frac{v(\mathbf{a})}{\langle v(\mathbf{a}) \rangle} d\mathbf{x} = \int_{\Omega(s)} \frac{v(\mathbf{x})}{\langle v(\mathbf{a}) \rangle} d\mathbf{x} = V_0, \tag{B12}$$

which implies that

$$\langle v(\mathbf{a}) \rangle = \frac{V(s)}{V_0} \left[\frac{1}{V(s)} \int_{\Omega(s)} v(\mathbf{x}) \mathrm{d}\mathbf{x} \right] = \frac{V(s)\langle v(\mathbf{x}) \rangle}{V_0}. \tag{B13}$$

Inserting this in equation (B10) gives

$$P(v,s) = \frac{1}{V_0} \frac{v}{\langle v(\mathbf{x}) \rangle} \frac{V_0}{V(s)} \int_{\Omega(s)} \delta[v - v_s(s,\mathbf{a})] \mathrm{d}\mathbf{x} = \frac{v}{\langle v(\mathbf{x}) \rangle} P_e(v,s). \tag{B14}$$

This shows that the ensemble s-Langrangian velocity PDF is related to the s-Eulerian velocity PDF through flux weighting.

B2. Relation Between the t-Eulerian Velocity PDF $P_e(v,t)$ and the Ensemble t-Lagrangian Velocity PDF $\hat{P}(v,t)$

Keeping the same spirit, we derive the relation between the Eulerian temporal velocity PDF $\hat{P}_e(v,t)$ and the ensemble temporal velocity PDF $\hat{P}(v,t)$. Starting with the definition of $\hat{P}(v,t)$:

$$\hat{P}(v,t) = \frac{1}{V_0} \int_{\Omega_0} \delta[v - v_t(t,\mathbf{a})] \mathrm{d}\mathbf{a}, \tag{B15}$$

and changing variable according to the map $\mathbf{a} \to \mathbf{x}(t,\mathbf{a})$, we obtain

$$\hat{P}(v,t) = \frac{1}{V_0} \int_{\Omega(t)} \mathbb{J}^{-1} \delta(v - v_e[\mathbf{x}(t,\mathbf{a})]) \mathrm{d}\mathbf{x}, \tag{B16}$$

$$\hat{P}(v,t) = \frac{1}{V_0} \int_{\Omega(t)} \delta(v - v_e[\mathbf{x}(t,\mathbf{a})]) \mathrm{d}\mathbf{x}, \tag{B17}$$

because the map is volume conserving and therefore $\mathbb{J} = 1$. And again from volume conservation $V_0 = V(t)$ which gives for equation (B17)

$$\hat{P}(v,t) = \frac{1}{V(t)} \int_{\Omega(t)} \delta(v - v_e[\mathbf{x}(t,\mathbf{a})]) \mathrm{d}\mathbf{x} = \hat{P}_e(v,t). \tag{B18}$$

B3. Relation Between the Ensemble s-Lagrangian Velocity PDF $P(v,s)$ and the Ensemble t-Lagrangian Velocity PDF $\hat{P}(v,t)$

Then, we can derive the relation between ensemble s-Lagrangian velocity PDF $P(v,s)$ and the ensemble t-Lagrangian velocity PDF $\hat{P}(v,t)$; starting with the definition of $\hat{P}(v,t)$ we have

$$\hat{p}(v,t) = \int_{\Omega_0} \delta(v - v_e[\mathbf{x}(t),\mathbf{a})]) \rho(\mathbf{a}) \mathrm{d}\mathbf{a}, \tag{B19}$$

$$= \int_{\Omega_0} \delta(v - v_e[\mathbf{x}(s(t),\mathbf{a})]) \rho(\mathbf{a}) \mathrm{d}\mathbf{a}, \tag{B20}$$

since $\mathbf{x}(t,\mathbf{a}) = \mathbf{x}(s(t),\mathbf{a})$. Then we can write it as

$$\hat{p}(v,t) = \int \int_{\Omega_0} \delta[s - s(t,\mathbf{a})] \delta[v - v_e(\mathbf{x}[s(t),\mathbf{a}])] \rho(\mathbf{a}) \mathrm{d}\mathbf{a}\mathrm{d}s. \tag{B21}$$

And then using the fact that

$$\delta[f(x)] = \sum_i \frac{1}{f'(x_i)} \delta(x - x_i), \tag{B22}$$

we obtain

$$\delta[s - s(t,a)] = \frac{1}{v_e[\mathbf{x}(s,\mathbf{a})]} \delta[t - t(s,\mathbf{a})]. \tag{B23}$$

Inserting this in equation (B21) leads to

$$\hat{p}(v,t) = \int \int_{\Omega_0} \frac{1}{v_e[\mathbf{x}(s,\mathbf{a})]} \delta[t - t(s,\mathbf{a})]] \delta[v - v_e[\mathbf{x}(s,\mathbf{a})]] \rho(\mathbf{a}) \mathrm{d}\mathbf{a}\mathrm{d}s, \tag{B24}$$

$$= \frac{1}{\nu} \int \int_{\Omega_0} \delta[t - t(s, \mathbf{a})] \delta[v - v_e[\mathbf{x}(s, \mathbf{a})]] \rho(\mathbf{a}) \mathrm{d}\mathbf{a} \mathrm{d}s. \tag{B25}$$

Then, recognizing that the inside integral is actually $p(v, t, s)$, that is, the joint PDF of time and velocity in space, we have

$$\hat{p}(v, t) = \frac{1}{\nu} \int p(v, t, s) \mathrm{d}s, \tag{B26}$$

where $p(v, t, s)$ is the joint PDF of velocity $v_s(s, \mathbf{a})$ and particle time $t(s, \mathbf{a})$,

$$p(v, t, s) = \int \delta[v - v_s(s, \mathbf{a})] \delta[t - t(s, \mathbf{a})] \rho(\mathbf{a}) \mathrm{d}\mathbf{a}. \tag{B27}$$

References

Alim, K., Parsa, S., Weitz, D. A., & Brenner, M. P. (2017). Local pore size correlations determine flow distributions in porous media. *Physical Review Letters*, *119*(14), 144501. https://doi.org/10.1103/physrevlett.119.144501

Batchelor, G. K. (2000). *An introduction to fluid dynamics*: Cambridge University Press.

Bear, J. (1972). *Dynamics of fluids in porous media*. New York: American Elsevier.

Becker, M. W., & Shapiro, A. M. (2003). Interpreting tracer breakthrough tailing from different forced-gradient tracer experiment configurations in fractured bedrock. *Water Resources Research*, *39*(1), 1024. https://doi.org/10.1029/2001WR001190

Benke, R., & Painter, S. (2003). Modeling conservative tracer transport in fracture networks with a hybrid approach based on the Boltzmann transport equation. *Water resources research*, *39*(11), 1324. https://doi.org/10.1029/2003WR001966

Berkowitz, B., Cortis, A., Dentz, M., & Scher, H. (2006). Modeling non-Fickian transport in geological formations as a continuous time random walk. *Reviews of Geophysics*, *44*, RG2003. https://doi.org/10.1029/2005RG000178

Berkowitz, B., & Scher, H. (2001). The role of probabilistic approaches to transport theory in heterogeneous media. In B. Berkowitz (Ed.), *Dispersion in heterogeneous geological formations* (Vol. 42, pp. 241–263). Dordrecht: Springer.

Bijeljic, B., & Blunt, M. J. (2006). Pore-scale modeling and continuous time random walk analysis of dispersion in porous media. *Water resources research*, *42*, W01202. https://doi.org/10.1029/2005WR004578

Bijeljic, B., Mostaghimi, P., & Blunt, M. J. (2011). Signature of non-Fickian solute transport in complex heterogeneous porous media. *Physical Review Letters*, *107*(20), 204–502.

Bijeljic, B., Muggeridge, A. H., & Blunt, M. J. (2004). Pore-scale modeling of longitudinal dispersion. *Water Resources Research*, *40*, W11501. https://doi.org/10.1029/2004WR003567

Carrel, M., Morales, V. L., Dentz, M., Derlon, N., Morgenroth, E., & Holzner, M. (2018). Pore-scale hydrodynamics in a progressively bioclogged three-dimensional porous medium: 3-D particle tracking experiments and stochastic transport modeling. *Water Resources Research*, *54*, 2183–2198. https://doi.org/10.1002/2017wr021726

Cvetkovic, V., Carstens, C., Selroos, J.-O., & Destouni, G. (2012). Water and solute transport along hydrological pathways. *Water resources research*, *48*, W06537. https://doi.org/10.1029/2011WR011367

Cvetkovic, V., Cheng, H., & Wen, X.-H. (1996). Analysis of nonlinear effects on tracer migration in heterogeneous aquifers using Lagrangian travel time statistics. *Water Resources Research*, *32*(6), 1671–1680.

Cvetkovic, V., Dagan, G., & Shapiro, A. (1991). An exact solution of solute transport by one-dimensional random velocity fields. *Stochastic Hydrology and Hydraulics*, *5*(1), 45–54.

Dagan, G. (1987). Theory of solute transport by groundwater. *Annual Review of Fluid Mechanics*, *19*, 183–215.

De Anna, P., Le Borgne, T., Dentz, M., Tartakovsky, A. M., Bolster, D., & Davy, P. (2013). Flow intermittency, dispersion, and correlated continuous time random walks in porous media. *Physical review letters*, *110*(18), 184–502.

De Anna, P., Quaife, B., Biros, G., & Juanes, R. (2017). Prediction of velocity distribution from pore structure in simple porous media. *Physical Review Fluids*, *2*(124), 103. https://doi.org/10.1103/PhysRevFluids.2.124103

de Josselin de Jong, G. (1958). Longitudinal and transverse diffusion in granular deposits. *Eos Transactions American Geophysical Union*, *39*, 67–74.

Delay, F., Ackerer, P., & Danquigny, C. (2005). Simulating solute transport in porous or fractured formations using random walk particle tracking. *Vadose Zone Journal*, *4*, 360–379.

Dentz, M., Cortis, A., Scher, H., & Berkowitz, B. (2004). Time behavior of solute transport in heterogeneous media: Transition from anomalous to normal transport. *Advances in Water Resources*, *27*(2), 155–173.

Dentz, M., Icardi, M., & Hidalgo, J. J. (2018). Mechanisms of dispersion in a porous medium. *Journal of Fluid Mechanics*, *841*, 851–882. https://doi.org/10.1017/jfm.2018.120

Dentz, M., Kang, P. K., Comolli, A., Le Borgne, T., & Lester, D. R. (2016). Continuous time random walks for the evolution of Lagrangian velocities. *Physical Review Fluids*, *1*(7), 74004.

Devroye, L. (1986). *Non-uniform random variate generation*. New York: Springer.

Gardiner, C. (2010). *Stochastic methods*. Berlin: Springer Verlag.

Gjetvaj, F., Russian, A., Gouze, P., & Dentz, M. (2015). Dual control of flow field heterogeneity and immobile porosity on non-Fickian transport in berea sandstone. *Water Resources Research*, *51*, 8273–8293. https://doi.org/10.1002/2015WR017645

Gotovac, H., Cvetkovic, V., & Andricevic, R. (2009). Flow and travel time statistics in highly heterogeneous porous media. *Water resources research*, *45*, W07402. https://doi.org/10.1029/2008WR007168

Gouze, P., Le Borgne, T., Leprovost, R., Lods, G., Poidras, T., & Pezard, P. (2008). Non-Fickian dispersion in porous media: 1. Multi-scale measurements using single-well injection withdrawal tracer tests. *Water Resources Research*, *44*, W06427. https://doi.org/10.1029/2007WR006278

Holzner, M., Morales, V. L., Willmann, M., & Dentz, M. (2015). Intermittent Lagrangian velocities and accelerations in three-dimensional porous medium flow. *Physical Review E*, *92*(1), 13015.

Hyman, J. D., Painter, S. L., Viswanathan, H., Makedonska, N., & Karra, S. (2015). Influence of injection mode on transport properties in kilometer-scale three-dimensional discrete fracture networks. *Water Resources Research*, *51*, 7289–7308. https://doi.org/10.1002/2015WR017151

Jin, C., Langston, P. A., Pavlovskaya, G. E., Hall, M. R., & Rigby, S. P. (2016). Statistics of highly heterogeneous flow fields confined to three-dimensional random porous media. *Physical Review E*, *93*, 13122.

Kang, P. K., de Anna, P., Nunes, J. P., Bijeljic, B., Blunt, M. J., & Juanes, R. (2014). Pore-scale intermittent velocity structure underpinning anomalous transport through 3-D porous media. *Geophysical Research Letters*, *41*, 6184–6190. https://doi.org/10.1002/2014GL061475

Kang, P. K., Dentz, M., Borgne, T. L., Lee, S., & Juanes, R. (2017). Anomalous transport in disordered fracture networks: Spatial Markov model for dispersion with variable injection modes. *Advances in Water Resources*, *106*, 80–94. https://doi.org/10.1016/j.advwatres.2017.03.024

Koponen, A., Kataja, M., & Timonen, J. (1996). Tortuous flow in porous media. *Physical Review E*, *54*(1), 406.

Kree, M., & Villermaux, E. (2017). Scalar mixtures in porous media. *Physical Review Fluids*, *2*(10), 104502. https://doi.org/10.1103/physrevfluids.2.104502

Kubo, R., Toda, M., & Hashitsume, N. (1991). *Statistical physics II, non-equilibrium statistical mechanics*. Heidelberg: Springer Verlag Berl.

Langevin, P. (1908). Sur la théorie du mouvement brownien. *Comptes rendus de l'Académie des Sciences (Paris)*, *146*, 530–533.

Le Borgne, T., de Dreuzy, J. R., Davy, P., & Bour, O. (2007). Characterization of the velocity field organization in heterogeneous media by conditional correlation. *Water Resources Research*, *43*, W02419. https://doi.org/10.1029/2006WR004875

Le Borgne, T., Dentz, M., & Carrera, J. (2008). Lagrangian statistical model for transport in highly heterogeneous velocity fields. *Physical Review Letters*, *101*(9), 90601. https://doi.org/10.1103/PhysRevLett.101.090601

Levy, M., & Berkowitz, B. (2003). Measurement and analysis of non-Fickian dispersion in heterogeneous porous media. *Journal of contaminant hydrology*, *64*(3), 203–226.

Liang, X., Lu, N., Chang, L.-C., Nguyen, T. H., & Massoudieh, A. (2018). Evaluation of bacterial run and tumble motility parameters through trajectory analysis. *Journal of Contaminant Hydrology*, *211*, 26–38. https://doi.org/10.1016/j.jconhyd.2018.03.002

Lumley, J. (1962). The mathematical nature of the problem of relating Lagrangian and Eulerian statistical functions in turbulence. *Mécanique de la Turbulence*, *108*, 17–26.

Matyka, M., Golembiewski, J., & Koza, Z. (2016). Power-exponential velocity distributions in disordered porous media. *Physical Review E*, *93*, 13110.

Meyer, D. W., & Bijeljic, B. (2016). Pore-scale dispersion: Bridging the gap between microscopic pore structure and the emerging macroscopic transport behavior. *Physical Review E*, *94*(1), 13107.

Morales, V. L., Dentz, M., Willmann, M., & Holzner, M. (2017). Stochastic dynamics of intermittent pore-scale particle motion in three-dimensional porous media: Experiments and theory. *Geophysical Research Letters*, *44*, 9361–9371. https://doi.org/10.1002/2017GL074326

Most, S., Bijeljic, B., & Nowak, W. (2016). Evolution and persistence of cross-directional statistical dependence during finite-Péclet transport through a real porous medium. *Water Resources Research*, *52*, 8920–8937. https://doi.org/10.1002/2016WR018969

Mostaghimi, P., Bijeljic, B., Blunt, M., et al. (2012). Simulation of flow and dispersion on pore-space images. *SPE Journal*, *17*(04), 1–131.

Noetinger, B., Roubinet, D., Russian, A., Le Borgne, T., Delay, F., Dentz, M., et al. (2016). Random walk methods for modeling hydrodynamic transport in porous and fractured media from pore to reservoir scale. *Transport in Porous Media*, *115*, 345–385.

Paganin, D., Mayo, S., Gureyev, T. E., Miller, P. R., & Wilkins, S. W. (2002). Simultaneous phase and amplitude extraction from a single defocused image of a homogeneous object. *Journal of microscopy*, *206*(1), 33–40.

Painter, S., & Cvetkovic, V. (2005). Upscaling discrete fracture network simulations: An alternative to continuum transport models. *Water Resources Research*, *41*, W02002. https://doi.org/10.1029/2004WR003682

Pollock, D. W. (1988). Semianalytical computation of path lines for finite-difference models. *Ground Water*, *26*(6), 743–750. https://doi.org/10.1111/j.1745-6584.1988.tb00425.x

Pope, S. B. (2000). *Turbulent flows*. Cambridge, UK: Cambridge University Press. https://doi.org/10.1017/CBO9780511840531

Risken, H. (1996). *The Fokker-Planck equation*. Berlin: Springer Verlag.

Saffman, P. (1959). A theory of dispersion in a porous medium. *Journal of Fluid Mechanics*, *6*(03), 321–349.

Sanchez, S., Ahlberg, P. E., Trinajstic, K. M., Mirone, A., & Tafforeau, P. (2012). Three-dimensional synchrotron virtual paleohistology: A new insight into the world of fossil bone microstructures. *Microscopy and Microanalysis*, *18*(5), 1095–1105.

Scher, H., Margolin, G., Metzler, R., Klafter, J., & Berkowitz, B. (2002). The dynamical foundation of fractal stream chemistry: The origin of extremely long retention times. *Geophysical Research Letters*, *29*(5), 1061. https://doi.org/10.1029/2001GL014123

Shapiro, A. M., & Cvetkovic, V. D. (1988). Stochastic analysis of solute arrival time in heterogeneous porous media. *Water Resources Research*, *24*(10), 1711–1718.

Siena, M., Riva, M., Hyman, J., Winter, C. L., & Guadagnini, A. (2014). Relationship between pore size and velocity probability distributions in stochastically generated porous media. *Physical Review E*, *89*(1), 13018.

Smal, P., Gouze, P., & Rodriguez, O. (2018). *An automatic segmentation algorithm for retrieving sub-resolution porosity from X-ray tomography images* (Vol. 166, pp. 198–207).

Taylor, G. I. (1921). Diffusion by continuous movements. *Proceedings of the london mathematical society*, *20*, 196–211.

Uhlenbeck, G. E., & Ornstein, L. S. (1930). On the theory of the Brownian motion. *Physical Review*, *36*(5), 823–841. https://doi.org/10.1103/physrev.36.823